Forschungszentrum Karlsruhe
in der Helmholtz-Gemeinschaft

Wissenschaftliche Berichte
FZKA 7338

Progress in Strength, Toughness and Lifetime Methods for Ceramics

T. Fett, G. Rizzi, M. Esfehanian, C. Volkert, M. Riva, S. Wagner, R. Oberacker

Institut für Materialforschung

Januar 2008

Forschungszentrum Karlsruhe

in der Helmholtz-Gemeinschaft

Wissenschaftliche Berichte

FZKA 7338

Progress in strength, toughness and lifetime methods for ceramics

T. Fett, G. Rizzi, M. Esfehanian *, C. Volkert, M. Riva *,

S. Wagner *, R. Oberacker *

Institut für Materialforschung

* Universität Karlsruhe, Institut für Keramik im Maschinenbau

Forschungszentrum Karlsruhe GmbH, Karlsruhe
2008

Forschungszentrum Karlsruhe GmbH
Postfach 3640, 76021 Karlsruhe

Mitglied der Hermann von Helmholtz-Gemeinschaft
Deutscher Forschungszentren (HGF)

ISSN 0947-8620

urn:nbn:de:0005-073382

Progress in strength, toughness, and lifetime methods for ceramics

Abstract:

For the characterization of the failure of ceramic materials the strength and the fracture toughness have to be determined. In the presence of subcritical crack growth, also lifetime measurements are of importance. Latest contributions by the authors shall be addressed by this report.

Part A will deal with strength computations for circular disks under sphere loading. Strength relations will be derived for the ball-on-ring test, the ball-on-3-balls test, and the recently developed 3-balls-on-3-balls test. As an application of the ball-on-3-balls test, stable crack extension found for coarse-grained alumina shall be discussed as an effect of an increasing crack growth resistance.

In **Part B,** a method will be proposed that allows for fracture toughness measurements on V-notched bending bars with a notch root radius of less than 0.1 µm. Due to the very small notch depths of about 40µm, the artificially introduced crack-like notches are comparable with natural cracks.

Part C will focus on a procedure for lifetime evaluation that allows for a multiple use of specimens which survived a preceding lifetime test on a lower load level. The related procedure will be applied to static lifetime measurements on SIALON in distilled water of 20°C.

Fortschritte auf dem Gebiet der Festigkeit, Risszähigkeit und Lebensdauer von Keramik

Kurzfassung:

Zur Charakterisierung des Versagensverhaltens keramischer Werkstoffe sind Festigkeits- und Risszähigkeitsmessungen erforderlich. Weist eine Keramik noch den Effekt des unterkritischen Risswachstums auf, sind auch Lebensdauermessungen unter statischer Belastung von großer Wichtigkeit. Neuere Beiträge der Autoren zur Untersuchungs-Methodik sind in diesem Bericht zusammengefasst.

Teil A befasst sich mit der Berechnung der maximalen Spannungen in runden Scheiben unter Kugelbelastung. Hierbei werden der “ball-on-ring test”, der “ball-on-3-balls test” und der kürzlich von den Verfassern entwickelte „3-balls-on-3-balls test“ betrachtet. Als praktische Anwendung der ermittelten Spannungen im “ball-on-3-balls test” wird das bei grobkörnigem Aluminiumoxid gefundene stabile Bruchverhalten als Effekt einer stark ansteigenden Risswiderstandskurve diskutiert.

In **Teil B** wird auf eine von den Verfassern entwickelte Methode eingegangen, die es gestattet, sehr kurze Kerben mit extrem kleinen Kerbradien zu erzeugen. Bei einer ZrO_2-Keramik konnten Kerbradien von unter 0.1 µm bei einer Kerbtiefe von nur 40µm erzeugt werden. Derartig kurze und scharfe Kerben sollten geeignet sein, das Verhalten natürlicher Risse in Keramiken anzunähern.

Schließlich wird in Teil C über eine Prozedur berichtet, die sich dafür eignet, eine vorhandene Anzahl an Lebensdauer-Versuchsproben optimal auszunutzen. Hierbei kann aus der erneuten Verwendung von auf niederem Lastniveau angefallenen „Durchläufern“ zusätzliche Information über das Risswachstumsgesetz gewonnen werden. Die Methode wird an Lebensdauermessungen von SIALON in destilliertem Wasser von 20°C demonstriert.

Contents

PART A

Evaluation of strength from tests on disks loaded by spheres (Stress relations and discussion of stable fracture)

A1. Multiaxial strength tests

In conventional strength or lifetime tests under tension, bending or compression loading, the uniaxial stress state prevails. In components, however, multiaxial stresses occur very often. Therefore, experimental methods were developed quite early to determine the strength and deformation behaviour of thin plates under multiaxial stress conditions.

The first developed test for circular disks is the ring-on-ring test. A disk-shaped specimen is supported by a ring and loaded by a concentric ring of smaller diameter. The test has been used extensively for strength measurements of glass and has been standardized. Whereas bending bars exhibit additional flaws at the edges, which are generated by the machining process, the edges of a circular disk are nearly free of stress and will not contribute to failure. For the ring-on-ring test, however, highly plane parallel disk-shaped specimens are required. If this is not the case, a 3-point contact between ring and specimen will occur. Only at a higher load will a continuous contact line develop, resulting in the correct stress distribution.

In order to avoid the undefined supporting conditions of the ring-on-ring test, the *ball-on-ring* test was developed [A1-A3]. In this test, a disk specimen is supported by a continuous or a ball-bearing ring and loaded centrally with a sphere. Besides the sphere-on-ring test, also the ball-on-3-balls test [A4-A6] is considered. Finally, a rather new test with 6 balls is addressed [A7, A8].

Ball-on-3-balls tests were carried out in a stiff loading device for soda-lime glass and a coarse-grained alumina. Whereas the tests on glass showed the expected spontaneous failure behaviour starting from the initial flaws, tests on Al_2O_3 exhibited typical features of stable crack extension well-known for macroscopic cracks in materials with an increasing crack growth resistance.

In order to interpret this effect unexpected for small natural cracks, stress intensity factors of semi-elliptical surface cracks were computed by application of the Rice equation [A9] in a procedure proposed by Cruse and Besuner [A10]. For these computations an analytical description for the stress distribution in the disk under ball-on-3-balls loading was applied. It can be concluded from the results that natural small cracks can propagate stably due to the strongly decreasing stresses with increasing distance from the disk center.

From the numerical computations it was concluded that under ball-on-3-balls loading, partially stable extension of naturally small initial cracks is possible in the same way that is well-known for macroscopic cracks. This explains the occurrence of non-linear load vs. displacement curves with pop-in events in the ball-on-3-balls strength tests.

A2. Stresses in sphere-loading tests

A2.1 Ball-on-ring test

In order to avoid undefined supporting conditions, the *ball-on-ring* test was developed. In this test, a disk specimen is supported by a ring and loaded centrally with a ball (see Fig. A1a). This test configuration was proposed by Shetty et al. [A1, A2]. To reduce friction effects between disk and supporting ring, the latter is sometimes replaced by a ball-bearing ring. The stress state in the centre region of the disk opposite to the loading sphere can be described by closed-form solutions as given in [A11,A12].

The main disadvantage of the tests with sphere loading is the somewhat unclear stress distribution at the tensile surface directly opposite the loading point, for which only approximate relations are available.

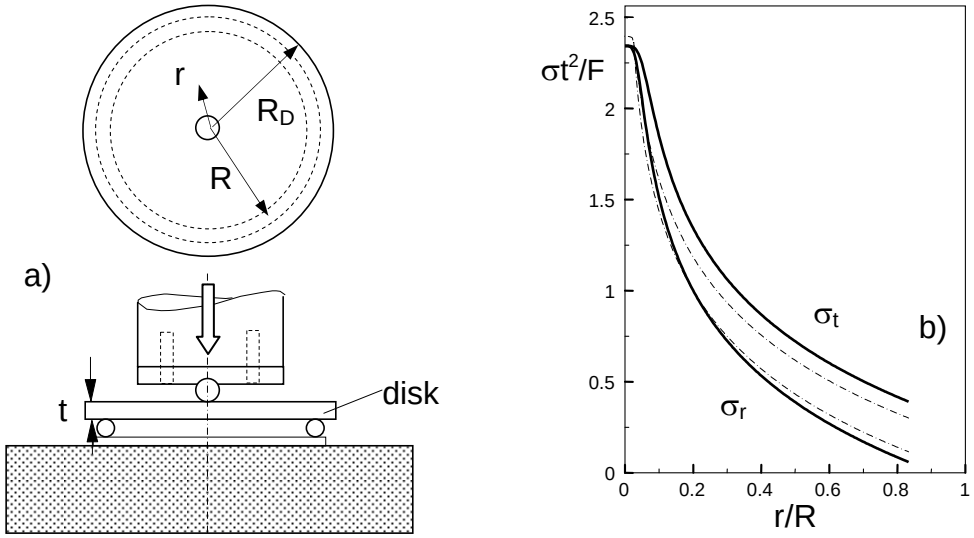

Fig. A1 a) Ball-on-ring test, b) stress distributions in the ball-on-ring test from FE computations by Shetty et al.[A1] (R/R_D=0.75, t/R_D=0.1, ν=0.3).

If the thickness of the disk is t, its radius R_D and the radius of the ball-bearing ring is R, the tangential and radial stresses on the tensile side can be expressed approximately as

$$\sigma_t = \frac{3F(1+\nu)}{4\pi t^2}\left\{2\ln(R/r) + \frac{1-\nu}{2(1+\nu)}\left[4 - \left(\frac{r_1}{r}\right)^2\right]\left(\frac{R}{R_D}\right)^2\right\}. \qquad \text{(A1a)}$$

$$\sigma_r = \frac{3F(1+\nu)}{4\pi t^2}\left\{2\ln(R/r) + \frac{1-\nu}{2(1+\nu)}\left[\left(\frac{R}{r}\right)^2 - 1\right]\left(\frac{r_1}{R_D}\right)^2\right\} \qquad \text{(A1b)}$$

(with ν=Poisson's ratio) as based on analytical work by Roark and Young [A11] and Vitman and Pukh [A13]. The two equations are valid for $r > r_1$ with the radius r_1 proportional to the plate thickness t [A1],

$$r_1 = \beta t \qquad \text{(A2)}$$

with $\beta \approx 1/3$. It is evident that the maximum stress in the plate centre depends strongly on the chosen value of the radius r_1.

From the finite element results by Shetty et al. [A1], re-plotted in Fig. 1b, it is obvious that a description by eqs.(1a) and (1b), shown as the dash-dotted lines, is very poor, especially in the case of tangential stresses. Whereas the solid lines in Fig. A1b represent the stresses from FE computations, the dash-dotted lines were obtained from (A1a) and (A1b) by using $r_1=t/3$. Let us improve the representation of the numerically obtained data.

Directly below the loading sphere, i.e. at $r=0$, an equi-biaxial stress must be present. From the condition $\sigma_r=\sigma_t$, it simply results for the coefficient β in (A2)

$$\beta = \frac{2R\alpha}{\sqrt{2R^2 - (\alpha t)^2}} \cong \sqrt{2}\alpha \tag{A3}$$

For strength tests, only the maximum principal stress σ_1, identical with the tangential stress σ_t is of importance very close to the disk centre. Therefore, let us define an effective radial coordinate r_{eff} to be inserted into (A1a), such that computed stresses agree with the FE results in the central region of the disk. From our FE computations, the fitting relation

$$\frac{r_{eff}}{R_D} = \sqrt{\left(\frac{r}{R_D}\right)^2 + \left(\alpha\frac{t}{R_D} + c\frac{R_D}{R}\right)^2} - c\frac{R_D}{R} \tag{A4}$$

is derived. This type of set-up was chosen in order to satisfy $r_{eff}=\alpha t$ and $d\sigma_t/dr=0$ for $r\to 0$. In principle, the unknown parameter α can be obtained from a single finite element run. In [A1] the finite element (FE) computations for $R/R_D=0.75$, $\nu=0.3$, and $t/R_D=0.1$ resulted in

$$\sigma_{max} = 2.35F/t^2 . \tag{A5}$$

This yields $\alpha=1/5$ and, consequently, $\beta=\alpha\sqrt{2}\cong 0.28$ in sufficiently good agreement with $\beta\cong 1/3$ as used in [1,2]. The shape parameter c has to be determined by additional FE computations. For the computation of the stresses, the radius r has to be replaced by the effective radius r_{eff} computed with these parameters.

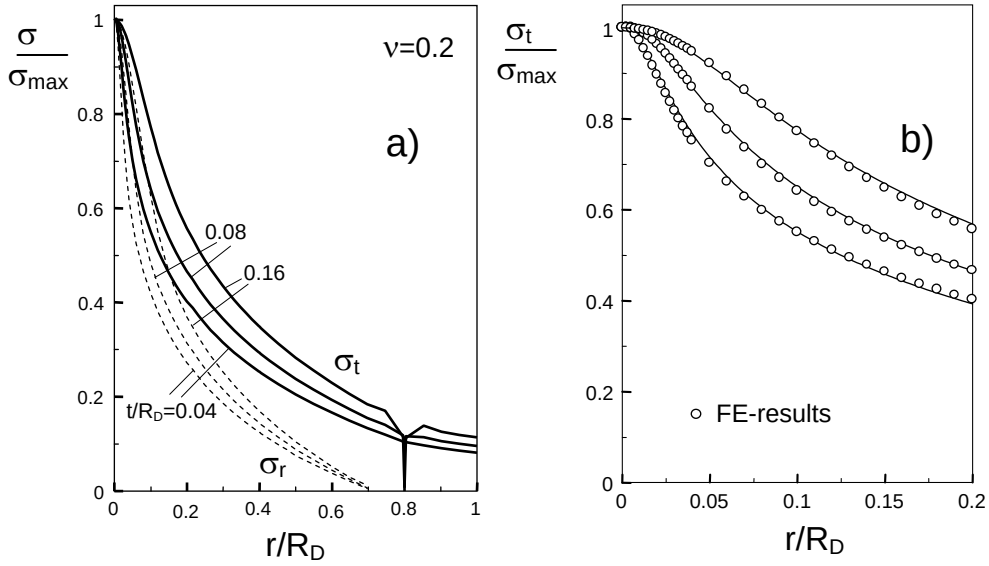

Fig. A2 a) Stress distributions in ball-on-ring tests for plates of R/R_D=0.8 and different thickness, b) comparison of the FE results (circles) for the tangential stress with the stress approximation given by eqs.(A1a), (A2)-(A4).

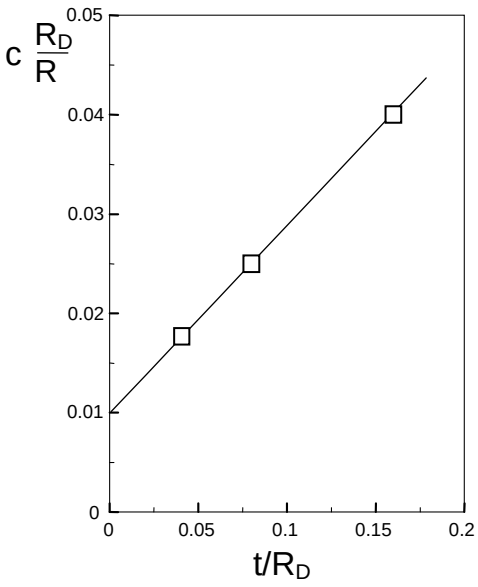

Fig. A3 Fitted values of the parameter *c* versus plate thickness *t*.

The maximum stress in the centre of the disk then reads by setting r=0 in eq.(A1a) and (A4)

$$\sigma_{\max} \cong \frac{3F(1+\nu)}{4\pi t^2}\left\{2\ln\left(\frac{R}{\alpha t}\right)+\frac{1-\nu}{1+\nu}\left(\frac{R}{R_D}\right)^2\right\} \tag{A6}$$

In Fig. A2, some FE results are shown for a plate of R/R_D=0.8 and varying thickness of t/R_D=0.04, 0.08, and 0.16. The tangential and radial stress components are plotted in Fig. A2a. Equation (A4) was fitted to the FE data for $r/R_D \le 0.15$ (Fig. A2b) yielding the unknown coefficient *c*. This value is plotted in Fig. A3 versus the plate thickness. The straight line in Fig. A3 can be expressed by

$$c\frac{R_D}{R} \cong 0.01 + 0.188\frac{t}{R_D} \tag{A7}$$

A comparison between FE results and fitting curve according to eqs.(A1a), (A4), and (A7) is shown in Fig. A2b. A possible influence of the ratio R/R_D is ignored assuming that this parameter will not deviate strongly from the changed value of 0.8 in all practical applications.

A2.2 Ball-on-3-balls test

Another test modification is the *ball-on-3-balls* configuration (Fig. A4a) described in [A4]. Here, the outer ring is replaced by 3 balls. This results in statically well-defined conditions, but a symmetric stress distribution no longer has to be expected. Closed-form analytical solutions for the case of supporting by a number of equally-spaced spheres along an outer circle are good approximations for the stress state at least for a large number of spheres [9]. Extensive computations of the stress state were given by Börger et al.[A5, A6]. Results from [A8] are given in Fig. A4b.

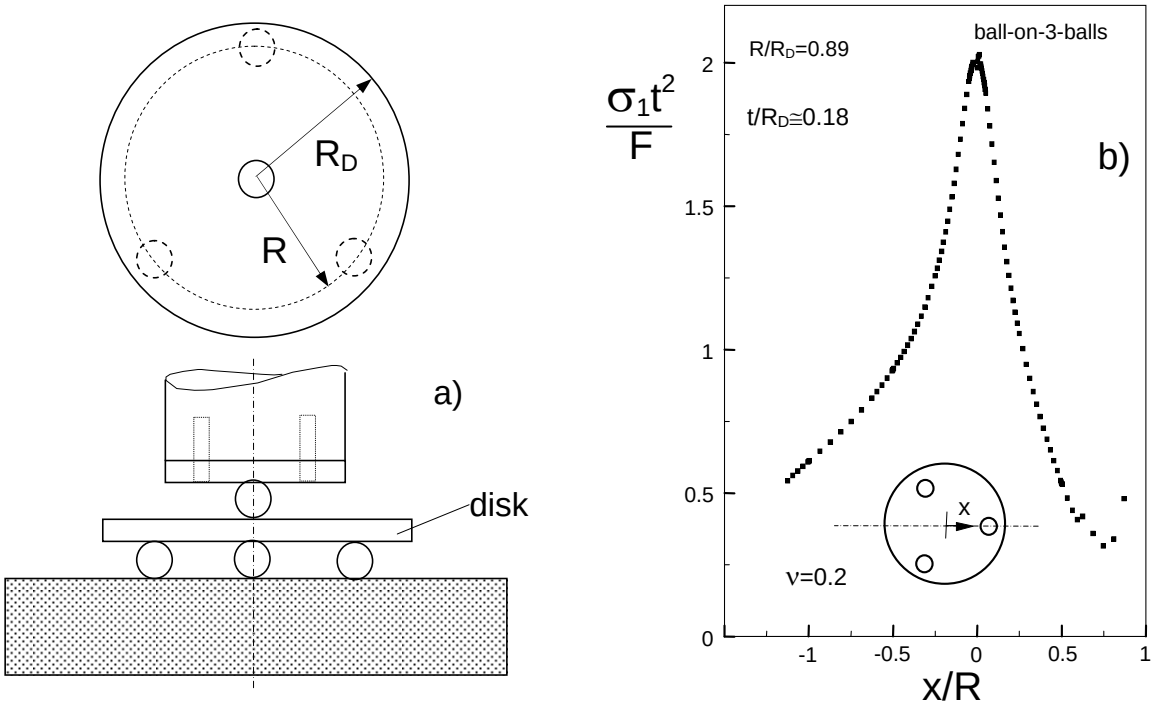

Fig. A4 a) Ball-on-3-balls test, b) FE results of the maximum stress component for a plate with R/R_D=0.89, t/R_D=0.178, ν=0.2 [A8].

The first principal stress (near the disk centre identical with the tangential stress component) can be computed approximately by using eqs.(A1a) and (A4) with the same values of α=1/5 and *c*. In Fig. A5a, the maximum stress at *r*=0 obtained from eq.(A6) is introduced as the circles. The straight lines represent FE results reported by Börger et al.[A5]. An excellent agreement is visible. Figure A5b shows the distribution of the maximum stress component as given by Börger et al.[A5] for a plate of t/R_D=0.2, R/R_D=0.87, and ν=0.3 as the circles. The open circles represent the first principal stress component along a line between the centre and point A, the solid circles between the centre and point B (see insert in Fig. A5b).

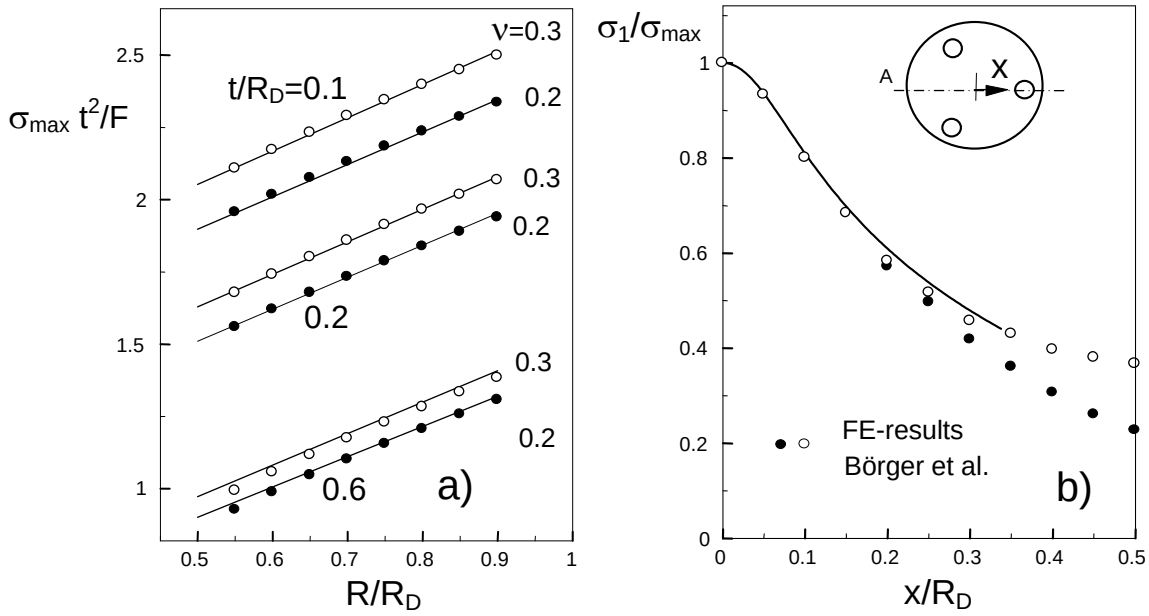

Fig. A5 Stresses for a disk in ball-on-3-balls loading, a) maximum stress at r=0 (symbols: eq.(A6), lines: fitted FE results of Börger et al. [A5]), b) distribution of the tangential stress component (line: computed with eq.(A1a) and (A4), open circles: results along the line between the centre and point A, solid circles: results along a line between the centre and point B.

Although the stresses in the ball-on-3-balls test are no longer symmetric with respect to the disk centre, the symmetric stress solution for the ball-on-ring test adequately describes also the stress state in this non-symmetric case. This can also be seen from the stress distribution of Fig. A4, re-plotted in Fig. A6.

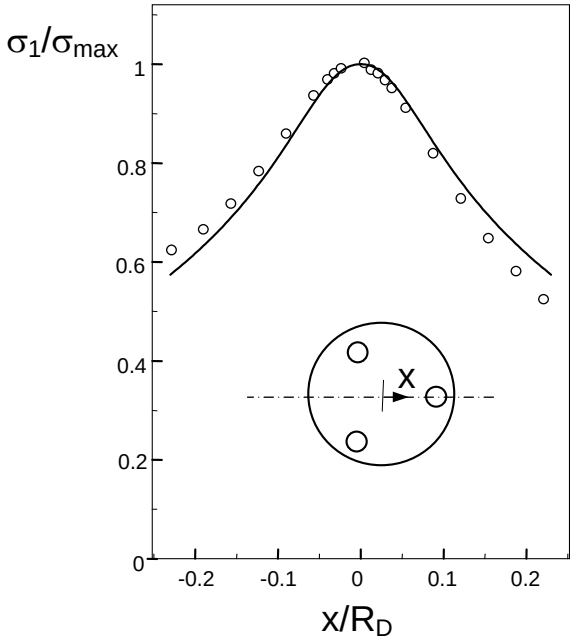

Fig. A6 Stresses for a disk in ball-on-3-balls loading; comparison of the approximated stresses (curve) with the FE results of Fig. A4b (circles).

A2.3 The 3-Balls-on 3-balls test

A2.3.1 Results from FE computations

In this chapter, a recently developed test using 3 loading and 3 supporting balls shall be addressed [A7, A8]. For this test, the maximum principal stresses and the biaxiality were determined for a wide range of geometries by using the finite element method. First experimental results obtained on glass and alumina are reported in [A8].

The main reason for the development of this test was to reduce the influence of the point-like stress spots and to obtain an increased effective surface tested. As shown in Fig. A7, the outer supporting and the inner loading forces are applied by 3 spheres each. By this configuration, mechanically well-defined supporting conditions as well as well-defined loading conditions are achieved.

In Fig. A7a, the loading and supporting spheres are „in line“, i.e. the sphere centres are located at the same polar angle. Figure A7b shows the case of the inner and outer spheres being shifted by an angle of φ=60°.

Figure A8 shows the disk of radius R_D and the sphere location circles R_1 (loading spheres) and R_2 (supporting spheres). The ratio of outer to inner sphere circles was chosen to be R_2/R_1=2.

Figure A9 presents the maximum principal stress σ_1 over the cross section A-A (see Fig. A9a). The influence of disk thickness t on the stresses is shown in Fig. A9b and A9c.

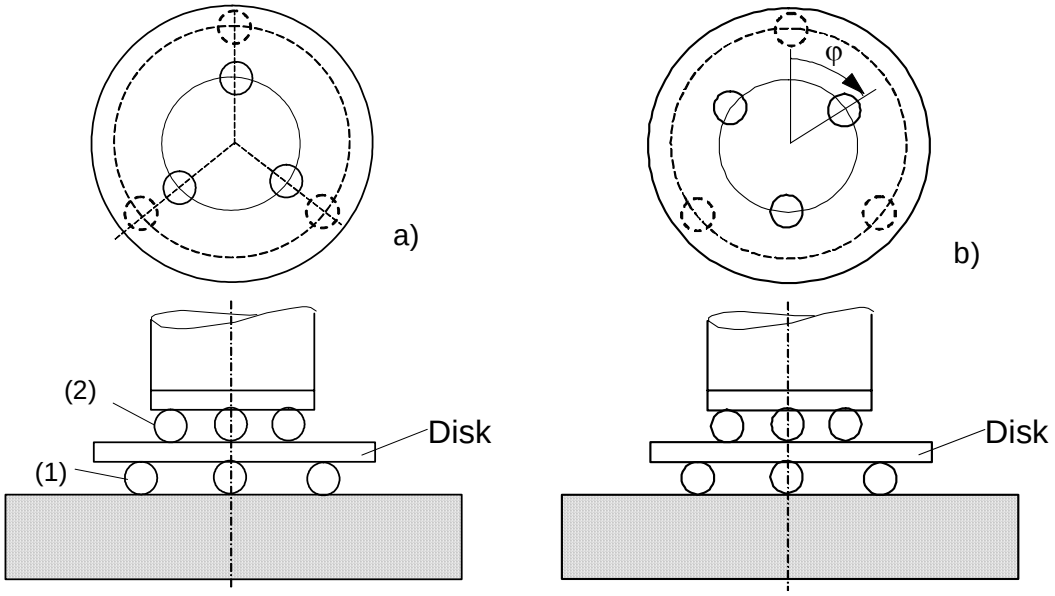

Fig. A7 3-balls-on-3-balls test: a) Loading and supporting spheres in line, b) loading and supporting spheres in line under an angle of φ=60°.

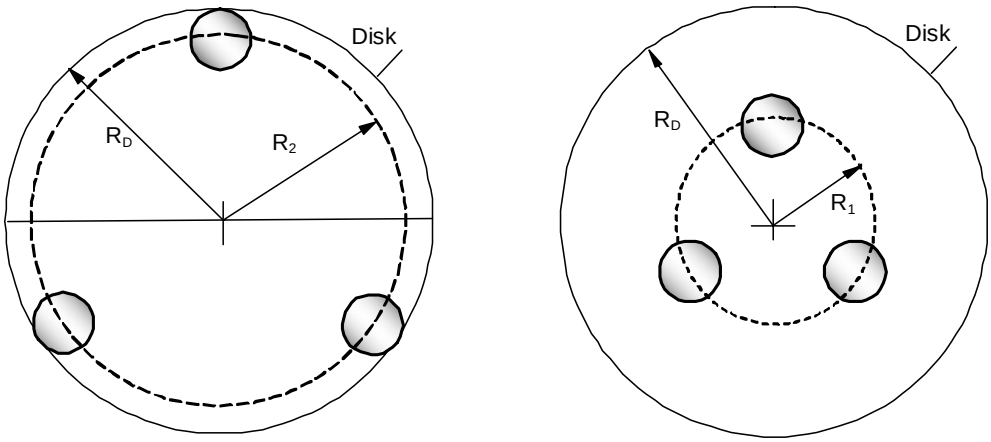

Fig. A8 Definition of the relevant radii R, R_1, and R_2.

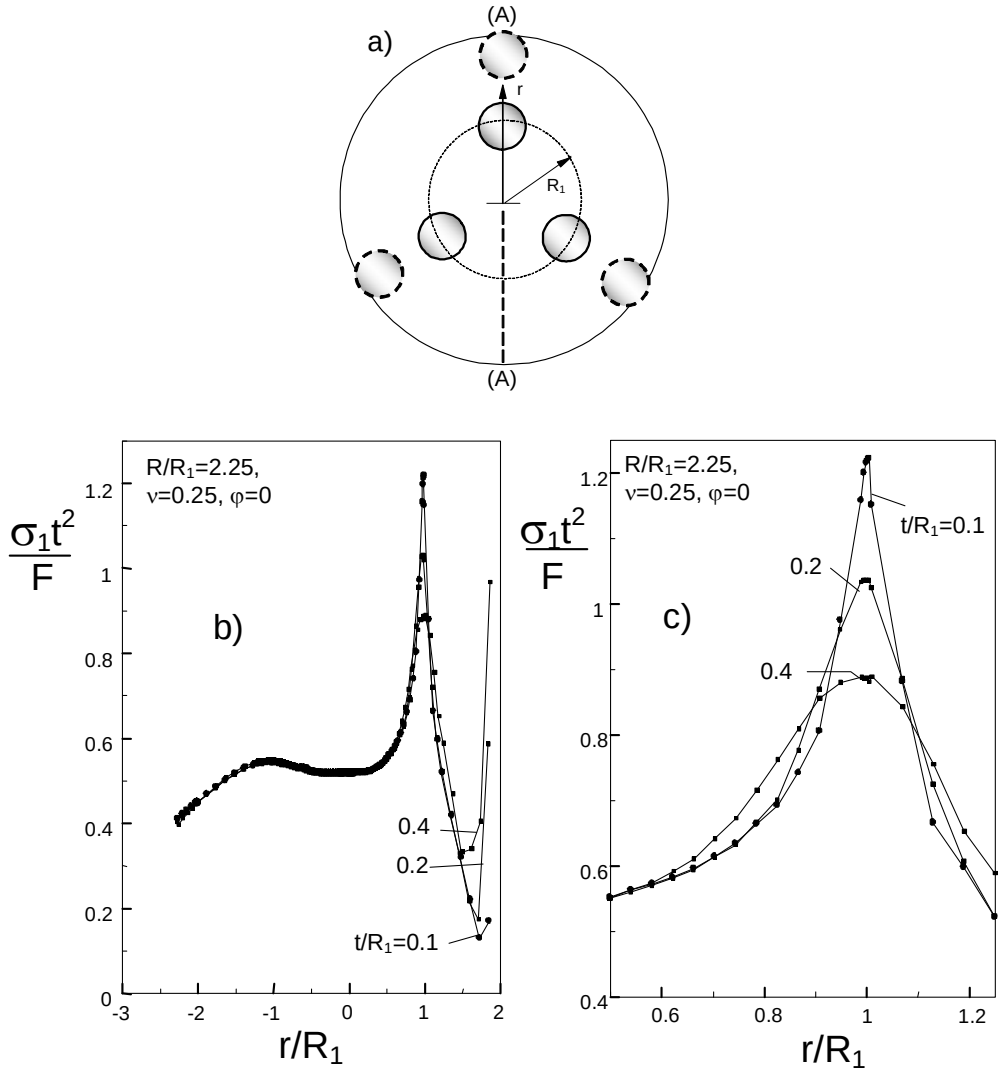

Fig. A9 Maximum principal stress for φ=0: a) loading situation (φ=0), b) and c) influence of the specimen thickness [A8].

Figures A10 shows the effect of Poisson's ratio ν for t/R_1=0.1. The maximum principal stress increases slightly with increasing ν. Figure A10c shows stresses for t/R_1=0.4.

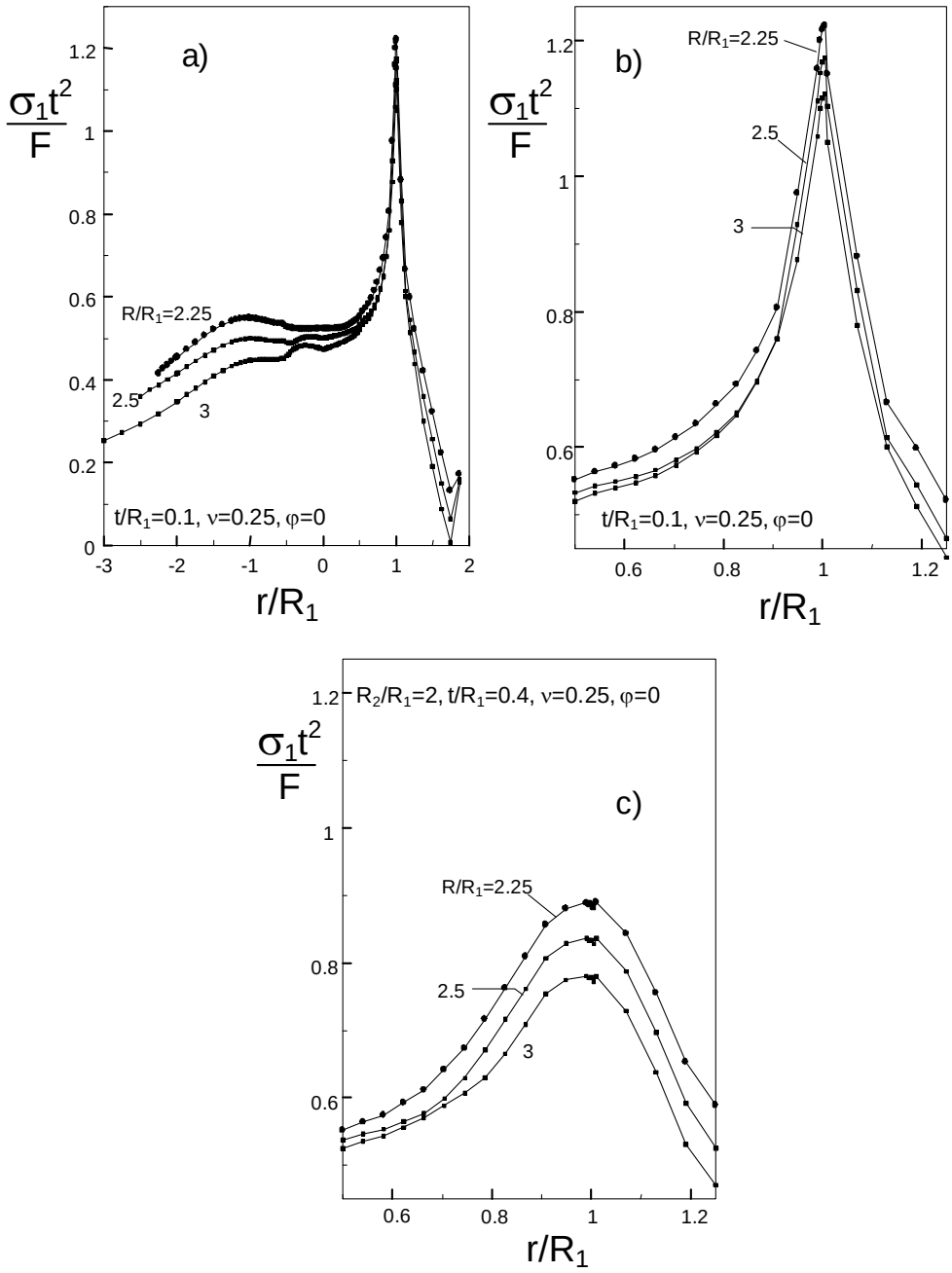

Fig. A10 Influence of the overhang on the maximum principal stress (φ=0°).

Figures A11 and A12 represent the stresses in the case of the inner balls being rotated by φ=60°.

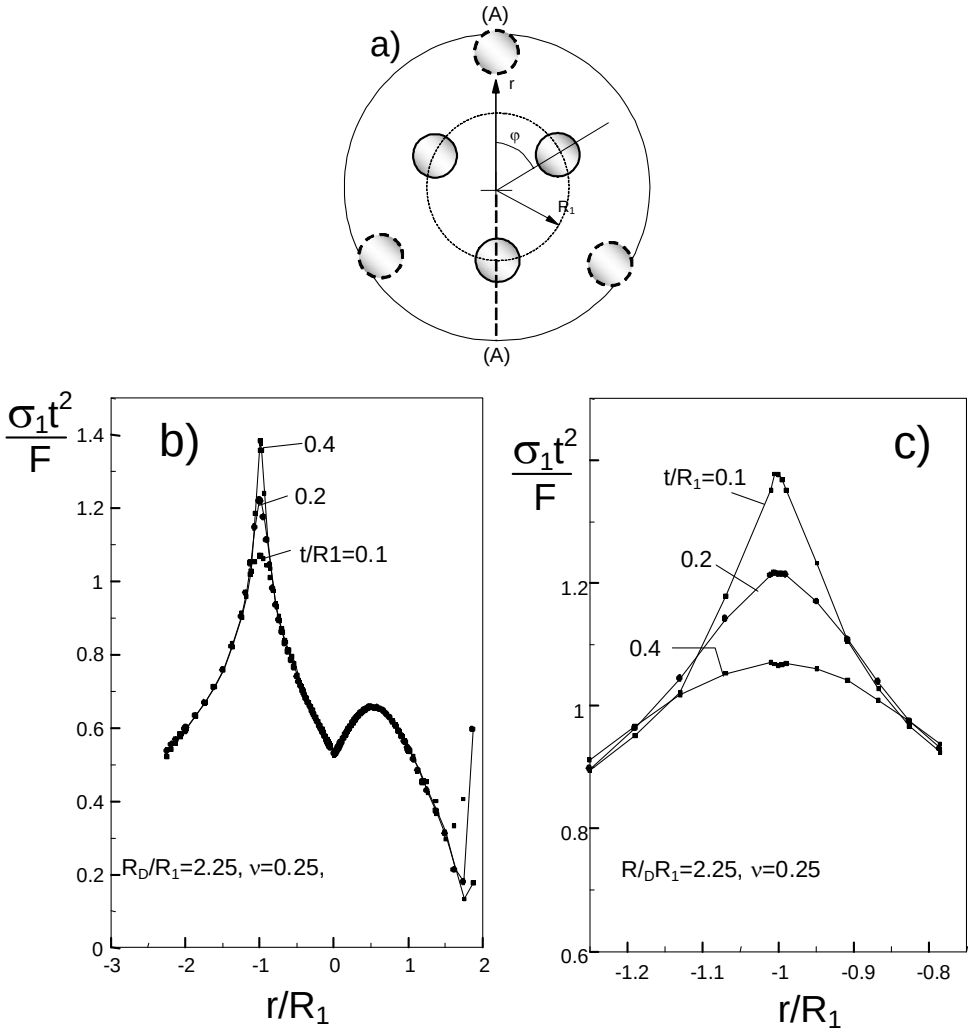

Fig. A11 Maximum principal stress along the line A-A for φ=60°: a) load application, b), c) Influence of specimen thickness.

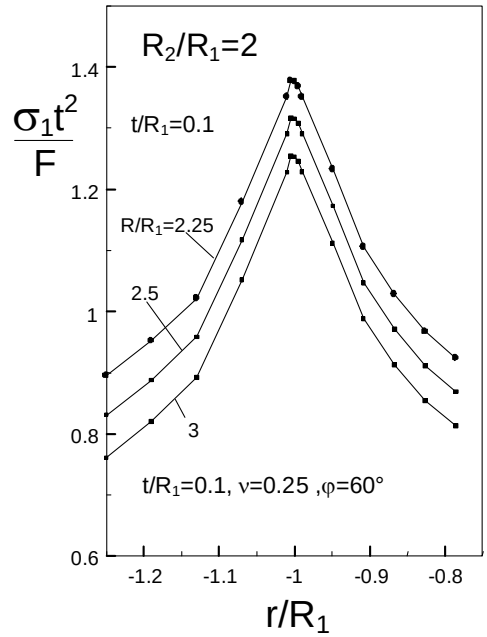

Fig. A12 Maximum principal stress along the line A-A for φ=60°: influence of the overhang.

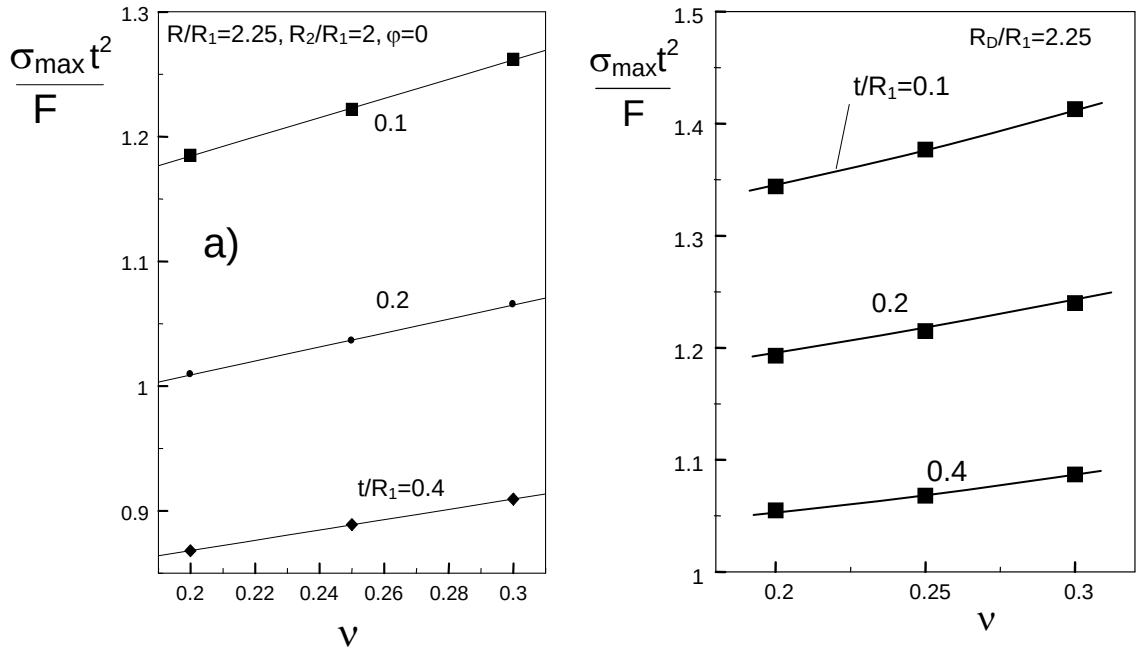

Fig. A13 Maximum values of the maximum principal stress as a function of Poisson's ratio ν, a) for φ=0, b) for φ=60°.

For the overhang of R/R_1=2.25, the final results are given in Fig. A13a for φ=0 and Fig. A13b for φ=60°.

For a disk with R/R_1=2.25, $0.1 \le t/R_1 \le 0.4$, and "sphere-in-line" conditions (φ=0), the FE results can be expressed by

$$\sigma_{1,\max}\frac{t^2}{F} = 0.656\left(\frac{t}{R_1}\right)^{-0.196} + 0.274\left(\frac{t}{R_1}\right)^{-0.448}\nu \qquad \text{(A8)}$$

For φ=60° and R_D/R_1=2.25, the maximum stress values can be approximated by

$$\sigma_{1,\max}\frac{t^2}{F} = 0.871\left(\frac{t}{R_1}\right)^{-0.142} + 0.197\left(\frac{t}{R_1}\right)^{-0.533}\nu \qquad \text{(A9)}$$

A2.3.2 Simplified fit relations

The same fit-procedure as mentioned in Sections A2.1 for the ball-on-ring test was applied to the stresses in a 3-balls-on-3-balls test. A simple fit according to

$$\sigma_{\max} \cong \frac{A_0 F(1+\nu)}{4\pi t^2}\left\{A_1 + 2\ln\left(\frac{R_1}{t}\right) + A_2\frac{1-\nu}{1+\nu}\left(\frac{R}{R_D}\right)^2\right\} \qquad \text{(A10)}$$

yields for the fixed geometry R_2/R_1=2 and ratios R_D/R_1 not too far away from R_D/R_1=2.5 (as recommended in [A8] for practical application)

A_0=1.22, A_1=4.221, A_2=8.304 for φ=0°

and

A_0=1.12, A_1=5.405, A_2=18.604 for φ=60°

A higher-order fit considering a wide range of R_D/R_1 results in coefficients A_1 and A_2 now as functions of R_D/R_1:

$$A_1 = 5.87 - 11.979\frac{R_1}{R_D} + 19.643\left(\frac{R_1}{R_D}\right)^2 \quad \text{for} \quad \varphi = 0° \tag{A11}$$

$$A_1 = 8.823 - 22.37\frac{R_1}{R_D} + 34.567\left(\frac{R_1}{R_D}\right)^2 \quad \text{for} \quad \varphi = 60° \tag{A12}$$

and

$$A_2 = 5.755 + 2.839\frac{R_D}{R_1} - 0.7279\left(\frac{R_D}{R_1}\right)^2 \quad \text{for} \quad \varphi = 0° \tag{A13}$$

$$A_2 = 4.851 + 5.487\frac{R_D}{R_1} \quad \text{for} \quad \varphi = 60° \tag{A14}$$

These dependencies are plotted in Fig. A14 for φ=0° and Fig. A15 for φ=60°.

Finally, the fitting curves according to eqs.(A10)-(A14) are shown in Fig. A16 together with the FE results given by the squares. The agreement is sufficient.

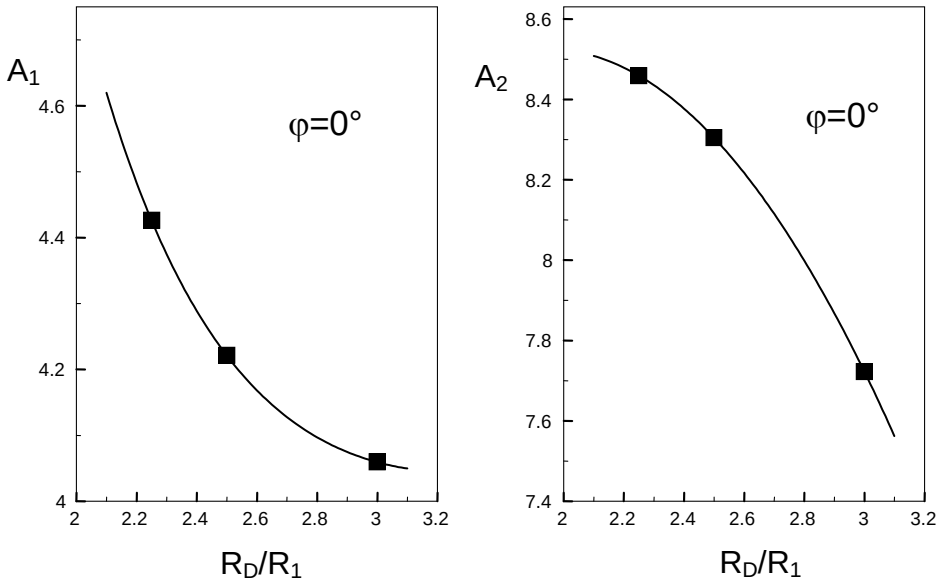

Fig. A14 Representation of the fitting curves eq.(A11) and (A13).

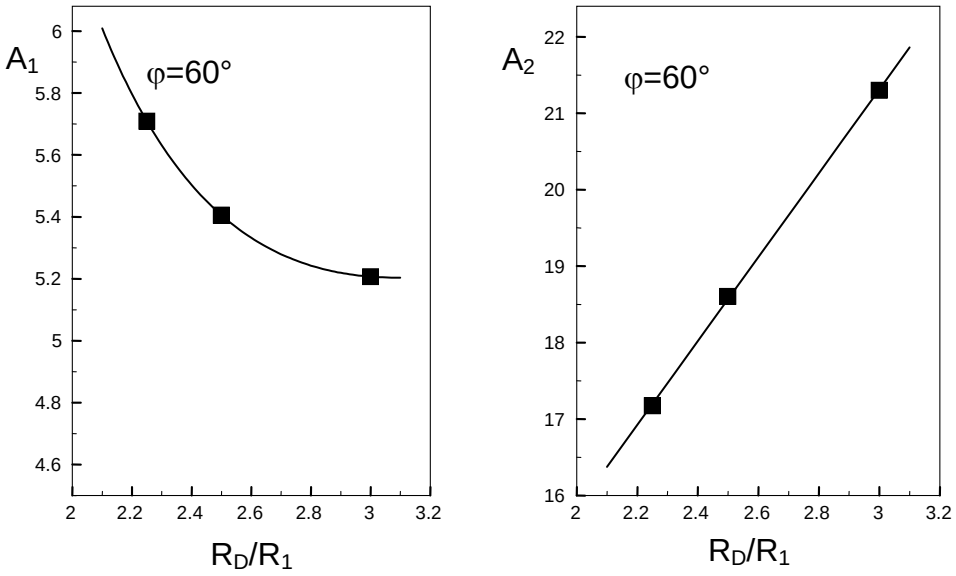

Fig. A15 Representation of the fitting curves eq.(A12) and (A14).

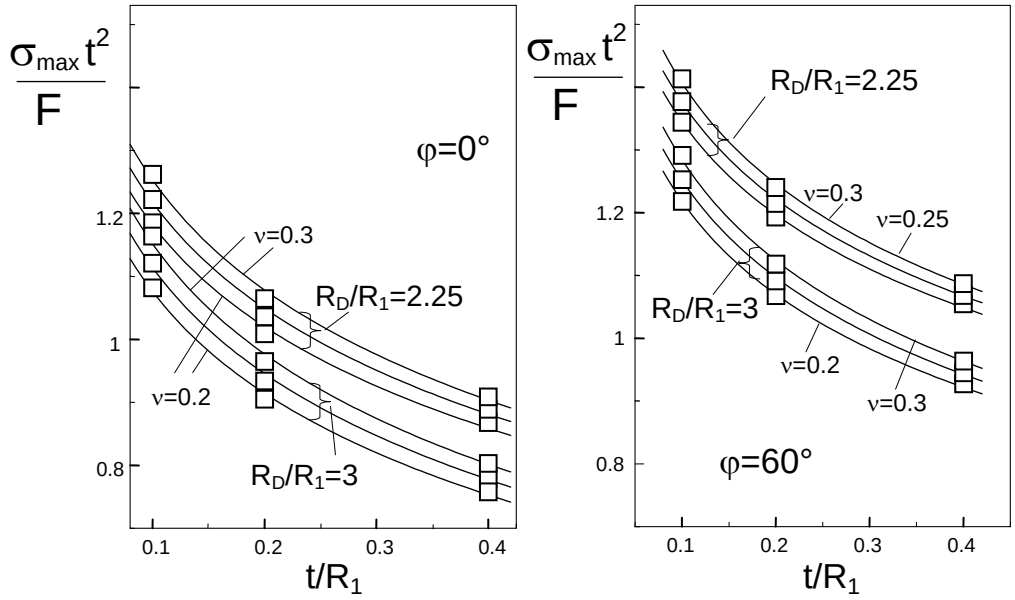

Fig. A16 Maximum values of the maximum principal stress as a function of Poisson's ratio ν, for φ=0 and φ=60°.

A3. Application of the ball-on-3-balls test

A3.1 Stable crack extension in tests on alumina

Biaxial flexure tests were carried out on 0.6 mm thick disks with a disk radius of R_D=8 mm. The supporting balls were arranged on a circle of R=5.5 mm in radius. Whereas disks made of soda-lime glass showed the expected spontaneous failure with a linear load-displacement curve (Fig. A17), coarse-grained alumina showed an F-δ curve, linear at low load, but curved increasingly at higher load, followed by several load pop-ins. This is a typical feature of stable crack extension phases. By unloading after the first pop-ins, macroscopic crack paths could be observed on the tensile surface. Crack penetration to the compressive surface was not detected before final fracture.

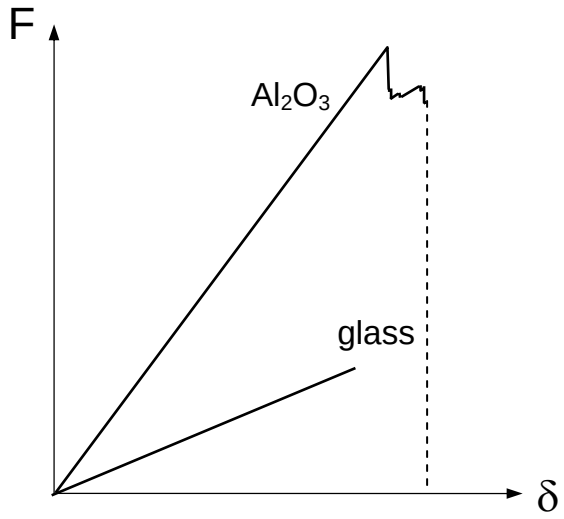

Fig. A17 Load versus displacement diagrams of disks made of coarse-grained alumina and soda-lime glass, obtained in a ball-on-3-balls test.

A3.2 Discussion of crack extension stability

A3.2.1 Stresses in the test specimens

In the special case of a ball-on-ring test, the stresses can be computed with good accuracy. The first principal stress (near the disk centre identical with the tangential stress component) can be computed approximately by using eq.(A1a) with the same values of α=1/5 and c given in (A4). Although the stresses in the ball-on-3-balls test are no longer symmetric with respect to the disk centre, the symmetric stress solution for the ball-on-disk test sufficiently describes also the stress state in this non-symmetric case. This can be seen from the stress distribution of Fig. A6.

From the FE results, it can be concluded that the depth distribution of the stresses is given as

$$\sigma(z) \cong \sigma_{z=0}(1-2z/t) \tag{A15}$$

with the origin of the z-coordinate, z=0, at the tensile surface of the disk. Small deviations from this linear relation occur in the centre region for z/t>0.9. In our computations, this region was without interest.

A3.2.2 Stress intensity factors

A simple fracture mechanics tool to describe the loading situation of semi-elliptical surface cracks is the computation of so-called averaged stress intensity factors. By applying this procedure, it is possible to determine averaged stress intensity factors on the basis of a relation of Rice [A9] which relates the variation of the crack opening displacement v_r in a certain reference loading case, e.g. σ_r=const., to the stress intensity factors in the current loading case σ. The subscript "*r*" denotes the reference loading case. It holds

$$\frac{1}{\Delta S}\int_{(\Delta S)} K_I\, K_{Ir}\, d(\Delta S) = E' \int_{(S)} \sigma \frac{\partial v_r}{\partial(\Delta S)}\, dS \tag{A16}$$

where $E' = E/(1-\nu^2)$, ν = Poisson's ratio, K_{Ir} is the reference stress intensity factor, and ΔS is a virtual increment of the crack area. The left-hand side of eq.(A16) allows to define the average stress intensity factor $\overline{K}$ [A10] according to

$$\overline{K}_I \overline{K}_{Ir} \Delta S = \int_{(\Delta S)} K_I K_{Ir}\, d(\Delta S) \tag{A17}$$

$$\overline{K}_{Ir} = \sqrt{\frac{1}{\Delta S}\int_{(\Delta S)} K_{Ir}^2\, d(\Delta S)} \tag{A18}$$

According to the right-hand side of eq.(A16), the average stress intensity factor can be computed from the actual stress distribution σ and the change of the crack opening displacement field v_r under the reference stress for the considered virtual increase of the crack

$$\overline{K} = \frac{E'}{\overline{K}_r} \int_{(S)} \sigma \frac{\partial v_r}{\partial(\Delta S)} dS \tag{A19}$$

A procedure for the determination of the crack opening displacement field for a semi-elliptic surface crack was outlined by Fett and Munz [A14].

Two independent virtual crack changes that preserve the semi-elliptical crack shape are possible (as proposed by Cruse and Besuner [A10]), namely, crack depth increment Δa with width c kept constant

$$\Delta S_A = \tfrac{1}{2}\pi c \Delta a \tag{A20}$$

or crack width increment Δc with depth a=const

$$\Delta S_B = \tfrac{1}{2}\pi a \Delta c \tag{A21}$$

as illustrated in Fig. A18.

The stress intensity factor corresponding to the constant stress contribution can be computed easily by application of the relation proposed by Newman and Raju [A15], which can be extended up to $a/c \cong 2.3$ (see e.g. [A14]).

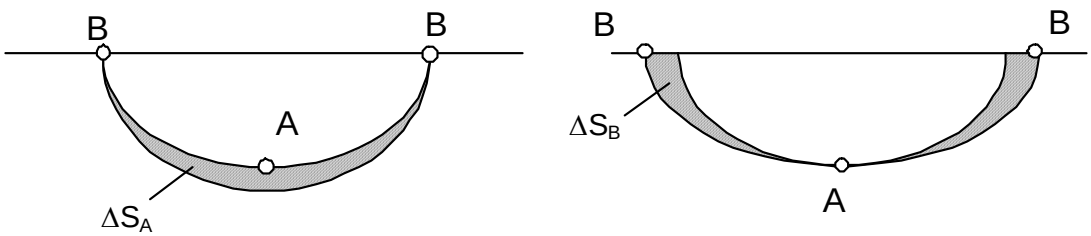

Fig. A18 Crack extension according to Cruse and Besuner [10].

In Figs. A19a and A19b, the stress intensity factors at the deepest point and at the surface points of the semi-elliptical crack are shown for the case of a disk under ball-on-3-balls loading.

The maximum possible stress intensity factors for the points (A) and (B) represented by the maxima of the envelopes are

$$\overline{K}_{A,\max} = 0.64\,\sigma\sqrt{t} \tag{A22a}$$

$$\overline{K}_{B,\max} = 0.60\,\sigma\sqrt{t} \tag{A22b}$$

In contrast to this behaviour, cracks in a plate under pure bending show monotonously increasing stress intensity factors for decreasing a/c without an envelope, see Fig. A20 (note the different scaling of the ordinate).

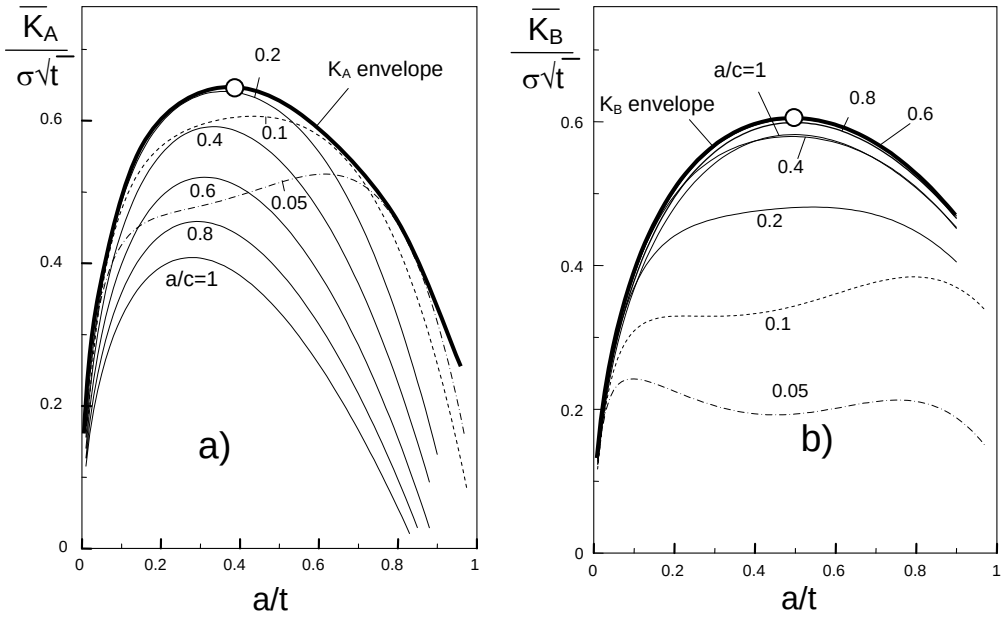

Fig. A19 a) Stress intensity factors for the deepest point (A) of semi-elliptical cracks under ball-on-3-balls loading together with the envelope of the single K_A curves (thick line), b) K values for the surface points (B).

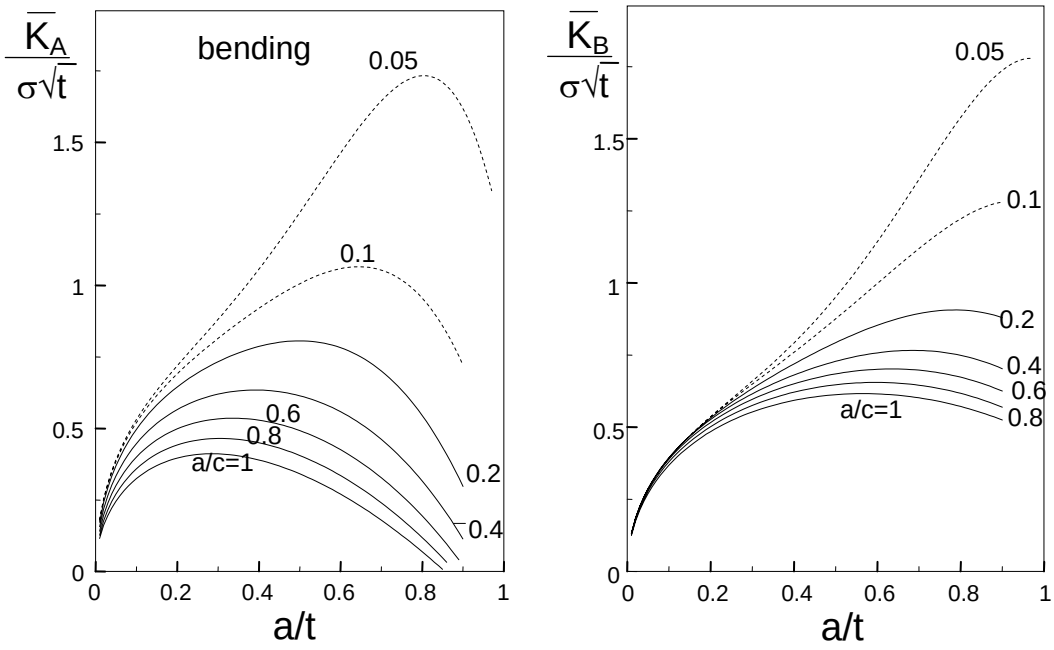

Fig. A20 a) Stress intensity factors for the deepest point (A) of semi-elliptical cracks under pure bending, b) *K* values for the surface points (B).

The occurrence of an envelope of stress intensity factors, which decreases at large values of *a* and *a*/*c* allows for stable crack extension to be detected under appropriate circumstances (e.g. a strongly rising crack resistance curve, R-curve).

A3.3 Crack extension behaviour

A3.3.1 Materials without R-curve behaviour

The crack growth behaviour of a material with constant crack growth resistance is illustrated in Fig. A21. Two natural semi-circular cracks of initial relative depths of a_0/t=0.05 and 0.1, i.e. a_0=30 and 60µm, are considered in Fig. A21a for the case of a ball-on-3-balls test. Under increasing stress σ (here, the maximum stress given by eq.(A1)), the stress intensity factor at point (A) increases, too. At the critical stress level $\sigma_{max}=\sigma_{max,c}$ resulting in

$$\frac{K_{I0}}{\sigma_{\max,c}\sqrt{t}} = \begin{Bmatrix} 0.24 & \text{for } a_0/t = 0.05 \\ 0.32 & \text{for } a_0/t = 0.1 \end{Bmatrix} \qquad \text{(A23)}$$

crack extension occurs. In eq.(A23), K_{I0} is the so-called crack tip toughness which is identical with the fracture toughness K_{Ic} in the absence of a rising fracture resistance.

Unstable crack growth occurs along the solid arrows until crack arrest takes place at least when the decreasing part of the K_A envelope is reached. In the case of the small crack, *a*=*t* is reached at this location; consequently, the crack cannot stop before complete fracture. But also in the case of the larger crack, crack arrest cannot be expected, although an intersection with the envelope is visible in Fig. A21a. Similar to the well-known crack extension in thermal shock experiments, there is an excess in the crack-driving energy, since $K>K_{I0}$ is always fulfilled during spontaneous crack extension. Due to the dynamic effects, the crack

can be driven beyond the K_A envelope as indicated by the dashed arrow. Also under these circumstances, complete fracture has to be expected. Figure A21b describes the crack extension in a bending test. Since no K_A envelope is present under pure bending, a crack must always extend to $a/t \rightarrow 1$, resulting in complete fracture (illustrated by the arrows).

From these considerations, it can be understood easily why glass did fracture spontaneously in all tests.

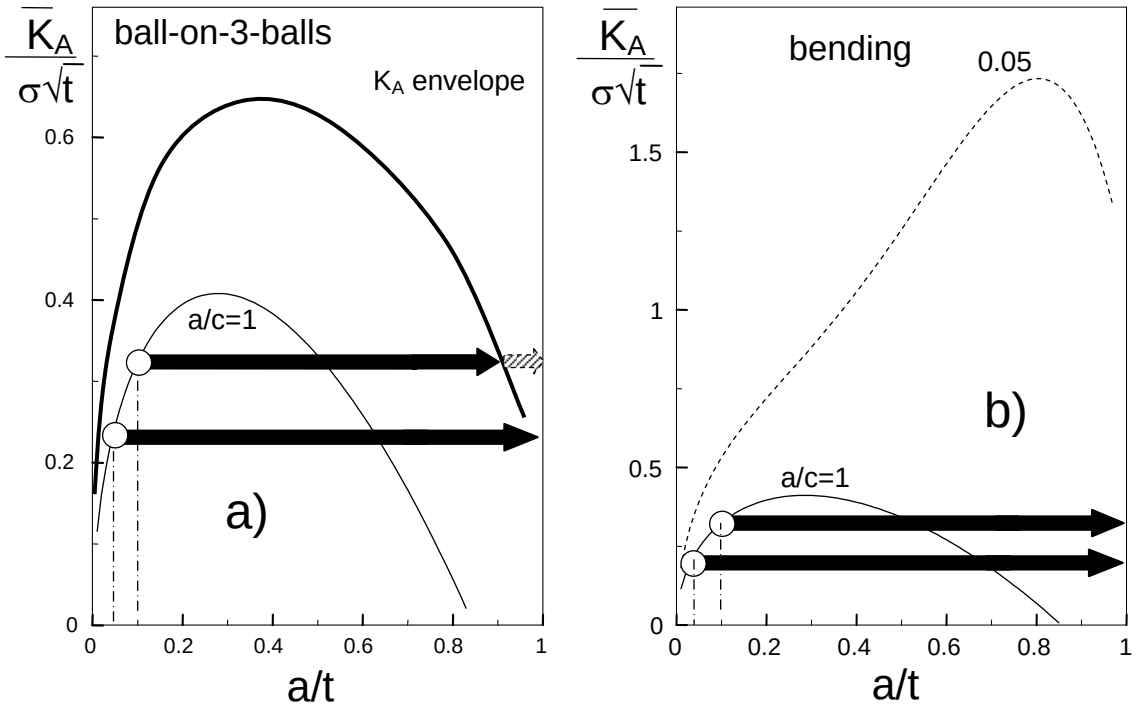

Fig. A21 Crack extension in materials with constant crack resistance a) under ball-on-3-balls loading, b) under pure bending.

A3.3.2 Materials with rising crack resistance curve

A characteristic feature of most ceramics is the existence of a rising crack growth resistance curve (R-curve), when the stress intensity factor during crack propagation increases from an initial value K_{I0} until a critical value is reached. The rising crack growth resistance of coarse-grained ceramics is caused by crack border interactions in the wake of the advancing crack. The stress intensity factor at the crack tip, K_{tip}, is the sum of K_{appl} from the external load and K_{sh} from the crack border interaction stresses:

$$K_{tip} = K_{appl} + K_{sh} \tag{A24}$$

During crack propagation, K_{tip} is constant and equals the so-called crack tip toughness K_{I0}. The shielding term K_{sh} is negative and increases with increasing crack extension. Therefore, K_{appl} must increase to maintain a constant K_{tip}.

A “steep” R-curve behaviour may be modelled by [A16]

$$K_{sh} = K_{sh,\max}[1 - \exp(-\lambda\sqrt{\Delta a})] \tag{A25}$$

For naturally small cracks at narrow notches, eqs.(A24) and (A25) were used in [A16] with the parameters $\lambda=40/\sqrt{m}$, $K_{sh,max}$ =-5 MPa$\sqrt{m}$, and K_{I0}=2.2 MPa$\sqrt{m}$. These data will be used also in the following analysis. Figure A22 shows the R-curve in the representation $K_{IR}=f(\Delta a, \Delta c)$.

Crack extension starts at a load σ_{max} for which the condition

$$\max(K_{appl,A}, K_{appl,B}) = K_{I0} \tag{A26}$$

is fulfilled for the first time at one of the locations A or B. If the R-curve is steep enough to satisfy the conditions

$$K_{appl,A}(a,c) = \sigma_{max} Y_A \sqrt{a} = K_{I0} - K_{sh,max}[1-\exp(-\lambda\sqrt{a-a_0}] \tag{A27a}$$

$$K_{appl,B}(a,c) = \sigma_{max} Y_B \sqrt{a} = K_{I0} - K_{sh,max}[1-\exp(-\lambda\sqrt{c-c_0}] \tag{A27b}$$

the crack will propagate in a stable manner, i.e. under increasing load $d\sigma_{max}>0$. Spontaneous crack extension starts, if eqs.(A27a, A27b) are fulfilled under the condition $d\sigma_{max}\leq 0$. Since the applied stress intensity factor during the spontaneous crack growth phase exceeds K_{I0}, dynamic effects are generated. Consequently, crack arrest after this phase cannot be computed by eqs.(A27a, A27b). Nevertheless, these relations can be applied to predict at least a *minimum* crack size after arrest.

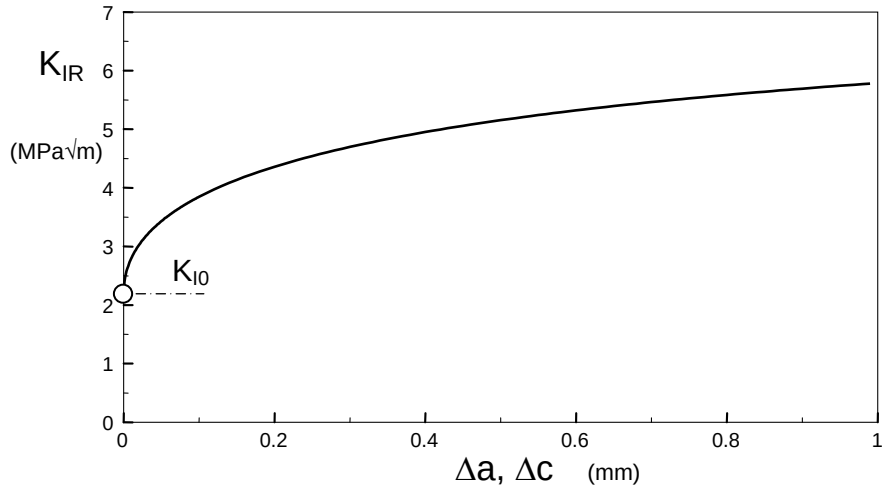

Fig. A22 R-curve according to eqs.(A14) and (A15) for $\lambda=40/\sqrt{m}$, $K_{sh,max}$ =-5 MPa$\sqrt{m}$, and K_{I0}=2.2 MPa$\sqrt{m}$.

The general procedure is illustrated for semi-elliptical cracks of initial depth a_0/t=0.1 (upper curves in Figs. A24a and A24b) assuming an R-curve according to eq.(A25) with λ=40 $m^{-1/2}$ and $K_{sh,max}$=-4 MPa$\sqrt{m}$. The semi-circular crack firstly fulfils condition (A26) for point B at about σ_{max}=270 MPa (open circle in Fig. A23a) and then propagates under increasing load to a depth of $a/t\cong 0.15$. During this phase, the aspect ratio a/c decreases monotonously, as shown in Fig. A23b. At a crack depth of $a/t\cong 0.15$ and a load of σ_{max}=315 MPa, the instability

condition $d\sigma_{max} \leq 0$ is satisfied. The crack then extends unstably along the arrow in Fig. A23a from the solid circle to the next open one.

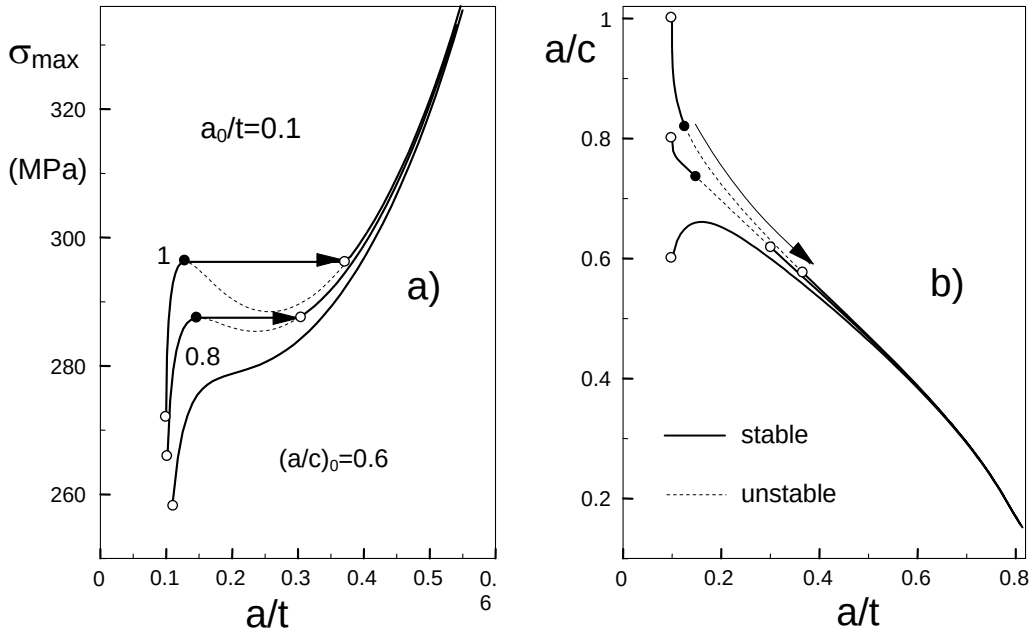

Fig. A23 Examples of crack development for an R-curve according to eq.(A25) with λ=40 $m^{-1/2}$ and $K_{sh,max}$=-4 MPa$\sqrt{m}$.

The solution of (A26a) and (A26b) would predict crack extension along the dashed parts of the curve. If the quasi-static equations are still applied in the unstable crack extension phase, i.e. by ignoring any dynamic effects, crack arrest has to be expected firstly at the open circles at the end of the arrows.

The further results in Fig. A23 are plotted tentatively. A behaviour similar to the initial semi-circular crack is found also for the crack with an initial aspect ratio of $(a/c)_0$=0.8. In contrast to the stable/unstable crack extension phases for $(a/c)_0$=0.8 and 1, an initial crack with $(a/c)_0$=0.6 shows completely stable crack propagation with the aspect ratio first increasing up to a crack depth of $a/t \cong 0.18$, followed by an increase in a/c.

Computations of an increased maximum shielding term of $K_{sh,max}$= -5 MPa$\sqrt{m}$ show that the same initial cracks as in Fig. A23 all propagate stably, as can be seen from Fig. A24a. In this representation, also smaller initial cracks with a_0/t=0.05 (a_0=30 µm) are included.

Figure A24b shows the cracks with a_0/t=0.1 in a bent plate of the same thickness. In this case, a significantly shorter stable crack extension phase is visible. The reason lies in the fact that a crack with large c-axis (i.e. with small aspect ratio a/c) cannot profit from a decreasing stress with increasing c as it is the case for the ball-on-3-balls test.

The effect of the R-curve parameters λ and $K_{sh,max}$ of eq.(A25) is illustrated in Fig. A25. From Fig. A25a, it can be seen that the stable crack extension phase decreases with decreasing λ. We can conclude that the steeper the R-curve firstly rises, the larger is the region of a/t, in which the crack can stably extend before final spontaneous fracture occurs. Figure A25b shows that stable crack propagation is enhanced for an increasing value of $|K_{sh,max}|$.

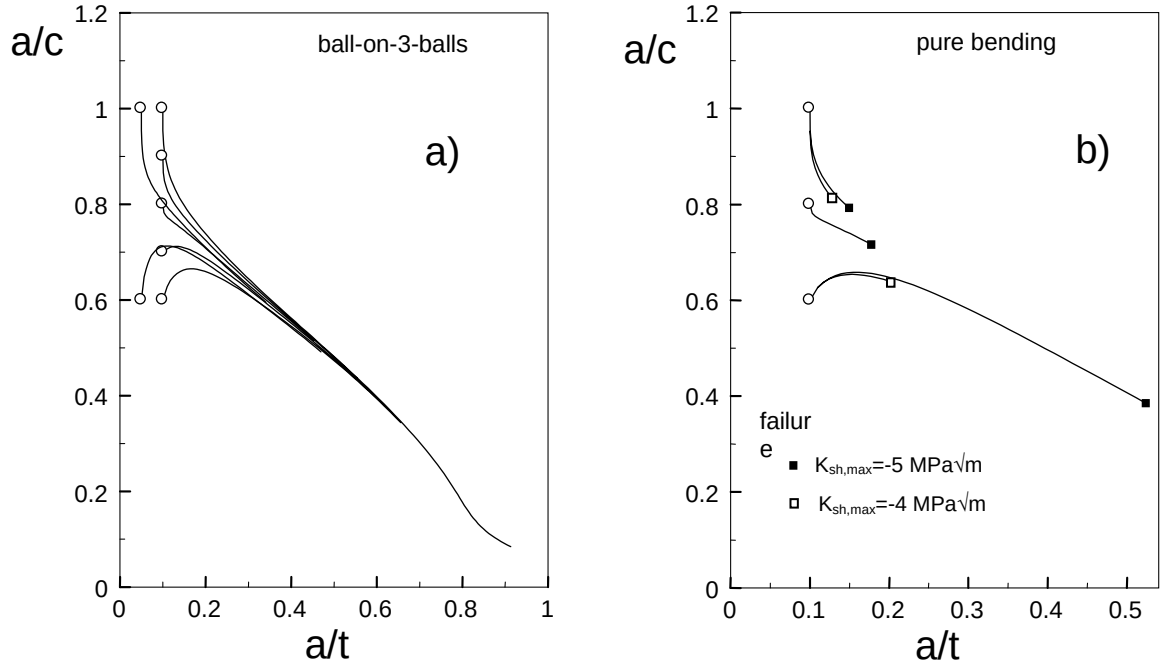

Fig. A24 a) Crack development for an R-curve according to eq.(A25) with λ=40 $m^{-1/2}$ and $K_{sh,max}$= -5 MPa√m in the ball-on-3-balls test, b) for cracks in a bent plate (thickness in both cases: t=0.6 mm), influence of $K_{sh,max}$ on the failure location.

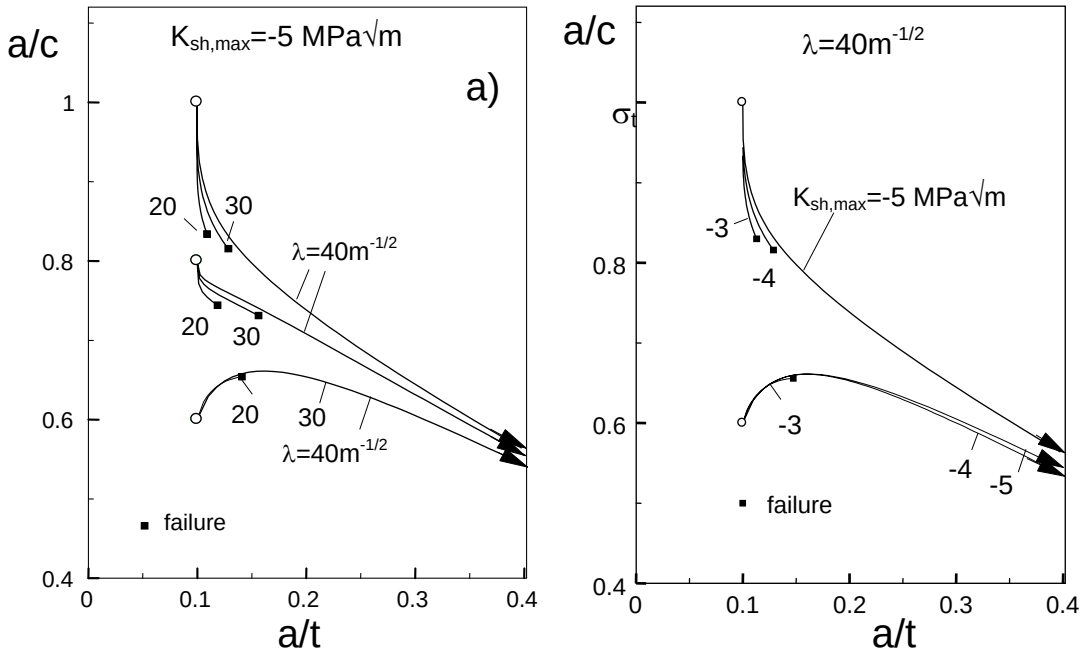

Fig. A25 Influence of the R-curve parameters a) λ and b) $K_{sh,max}$ on the stable crack extension phase in the ball-on-3-balls test, c) influence of the plate thickness at a constant crack depth of a_0=60 µm.

Summarizing the computations of Sections A3.2 and A3.3 we can conclude that under ball-on-3-balls loading, partially stable extension of naturally small initial cracks is possible in the same way that is well-known for macroscopic cracks. This explains the occurrence of non-linear load vs. displacement curves with pop-in events in the ball-on-3-balls strength tests.

A4. Displacements in ball-on-3-balls tests

The ball-on-3-balls tests give the possibility to determine the Young's modulus from the load vs. loading-point displacements. The plate displacements δ between the plate centre and the supporting points (evaluated at locations A and B in half thickness, see Fig. A26a) were evaluated for t/R=0.05 and 0.1. The data can be expressed by

$$\delta = \psi \frac{FR^2}{Et^3} \tag{A28}$$

with the coefficient ψ plotted in Fig. A26b for t/R=0.05 and different values of the Poisson's ratio as a function of the overhang R_D/R. For ν=0.25, $t/R \leq 0.1$, and $1.12 < R_D/R < 1.5$, the approximation relation holds

$$\psi \cong 0.898 - 1.19\frac{R}{R_D} + 1.0782\left(\frac{R}{R_D}\right)^2 \tag{A29}$$

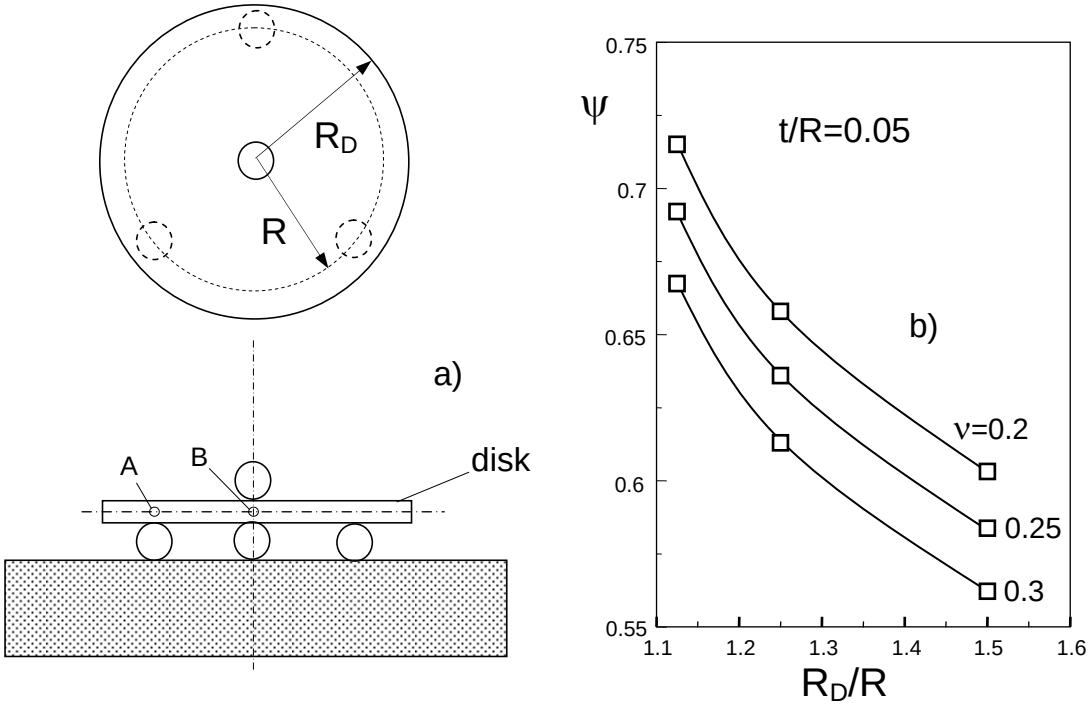

Fig. A26 Plate displacements: a) geometry, b) normalized displacements according to eq.(A28) as a function of the plate overhang.

References of Part A

[A1] Shetty, K.D., Rosenfield, A.R., McGuire, P., Duckworth, W.H., Biaxial flexure test for ceramics, Amer. Ceram. Soc. Bulletin **59** (1980), 1193-1197.

[A2] Shetty, K.D., Rosenfield, A.R., McGuire, P., Bansal, G.K., Duckworth, W.H., Biaxial fracture studies of a glass ceramic, J. Amer. Ceram. Soc. **64** (1981), 1-4.

[A3] de With, G., Wagemans, H.H.M., Ball-on-ring test revisited, J. Amer. Ceram. Soc. **72** (1989), 1538-1541.

[A4] Godfrey, D. J. and John, S., Disc flexure tests for the evaluation of ceramic strength, In *Proceedings 2nd International Conference of Ceramic Materials and Components for Engines*. Verlag Deutsche Keramische Gesellschaft, Lübeck-Travemünde, 14–17 April 1986, pp. 657–665.

[A5] Börger, A., Supancic, P., Danzer, R., The ball on three balls test for strength testing of brittle discs: stress distribution in the disc, J. Europ. Ceram. Soc. **22** (2002), 1425-1436.

[A6] Börger, A., Supancic, P., Danzer, R., The ball on three balls test for strength testing of brittle discs: Part II: analysis of possible errors in the strength determination**,** J. Europ. Ceram. Soc. **24** (2004), 2917-2928.

[A7] Fett, T., Rizzi, G., A 3-balls-on-3-balls test for ceramic disks: A finite element study, Report FZKA 7052, Forschungszentrum Karlsruhe, Karlsruhe 2004.

[A8] Fett, T., Rizzi, G., Ernst, E., Müller, R., Oberacker, R., A 3-balls-on-3-balls strength test for ceramic disks, J. Europ. Ceram. Soc., 27(2007), 1-12.

[A9] Rice, J.R., Some remarks on elastic crack-tip stress fields, Int. J. Solids and Structures **8**(1972), 751-758.

[A10] Cruse, T.A., Besuner, P.M., Residual life prediction for surface cracks in complex structural details, J. of Aircraft **12**(1975) 369-375.

[A11] Roark, R.J., Young, W.C., Formulas for Stress and Strain, 5th Edition, McGraw Hill, 1975.

[A12] Szilard, R., Theory and Analysis of Plates, Prentice-Hall, 1974.

[A13] Vitman, F.F., Pukh, V.P., A method for determining the strength of sheet glass, Zavod. Lab, **29**(1963), 863-867.

[A14] Fett, T., Munz, D., Stress intensity factors and weight functions, Computational Mechanics Publications, 1997, Southampton.

[A15] Newman, J.C., Raju, I.S., An empirical stress intensity factor equation for the surface crack, Engng. Fract. Mech. **15**(1981) 185-192.

[A16] Fett, T., Influence of a finite notch root radius on fracture toughness, J. Europ. Ceram. Soc. 25(2005), 543-547.

PART B

A fracture toughness test using extremely sharp small notches

B1. Fracture toughness and R-curve

Fracture toughness measurements are often carried out with pre-notched specimens. Frequently, the notches are introduced by thin saw cuts or produced with the razor blade procedure as proposed by Nishida et al. [B1] and successfully applied by Kübler [B2]. With this procedure relatively small notch radii of about 3-4 µm are reached. However, toughness measurement with V-notches meets with some difficulties:

a) *Finite notch root radius*: If a_0 is the depth of the notch and ℓ the length of an edge crack propagating from the notch root (for the geometric data see Fig. 1a), the stress intensity factor is commonly computed formally as the stress intensity factor of a crack of total length $a=a_0+\ell$, i.e.

$$K^* = \sigma_{bend} \sqrt{\pi(a_0 + \ell)}\, F_{bend}(a/W) \qquad \text{(B1)}$$

where F_{bend} is the geometric function of an edge crack of length a in a specimen of width W under the applied load, for instance, under a bending load. For many geometric and loading situations, the geometric function F is available from fracture mechanics handbooks.

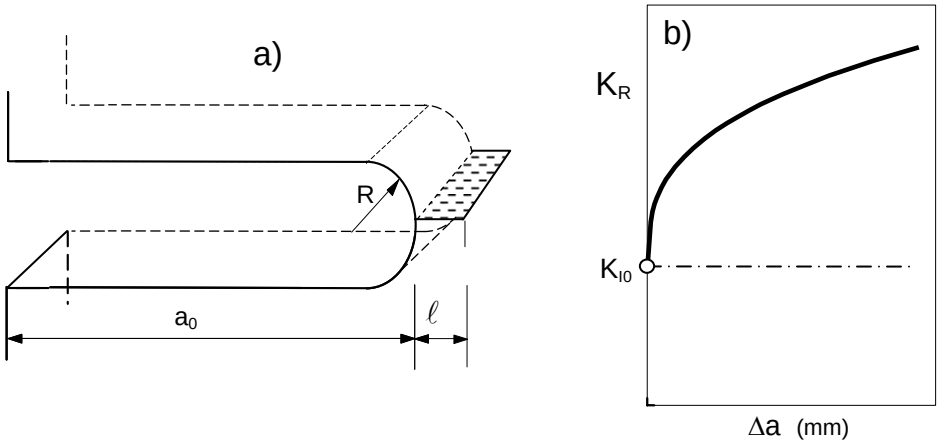

Fig. B1 a) Edge crack in front of a notch, b) crack-tip toughness K_{I0} as the starting point of the R-curve.

The stress intensity factor K^* given by eq.(B1) is correct only when the crack length ℓ is much larger than the radius of the notch R. In the first phase of crack extension, in which the crack length ℓ is comparable with R, the quantity K^* deviates strongly from the correct stress intensity factor K. In this case, the fracture mechanics problem of a small crack in front of a finite notch has to be considered. In the special case of an edge crack ahead of a slender notch with R being small compared to the notch depth a_0 and the other specimen dimensions, the true stress intensity factor K is given by [B3]

$$K \cong K^* \tanh[2.243\sqrt{\ell / R}] \qquad \text{(B2)}$$

From this relation, it is clearly visible that the true stress intensity factor is significantly lower than the formally computed values K^*. On the other hand, it can be concluded that notch effects are of importance for $\ell < R$ only.

As a rough estimation, Damani et al. [B4, B5] assumed a pre-existing crack at the notch root, which is proportional to the mean grain size d_m, with $\ell \approx 2\text{-}3d_m$, since grain boundaries may act as crack-like defects. This implies that a preparation of extremely sharp notches is of importance only for fine-grained ceramics with $d_m < 1\text{-}2\mu m$.

b) *Influence of the type of R-curve*: Failure of ceramics is often affected by the crack-growth resistance curve, the so-called R-curve (Fig. B1b). This behaviour is somewhat complicated, since R-curves of naturally small cracks are different from those of macroscopic cracks. Many experimental results from literature show the trend of lower R-curves with a steeper initial increase for the small cracks. A survey of data is given by Munz [B6], confirming that this seems to be the general case. Figure B2, for instance, presents R-curves of MgO-doped zirconia and coarse-grained alumina for large and small cracks.

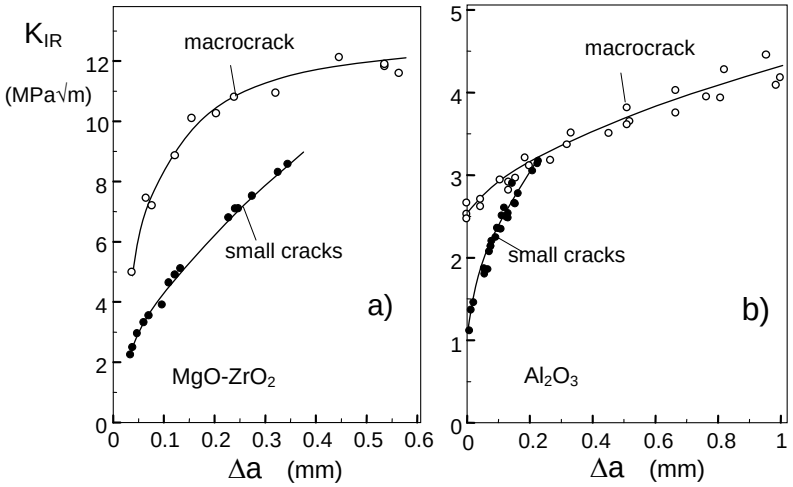

Fig. B2 R-curves for small and large cracks (macrocracks), a) MgO-doped zirconia [B7], b) coarse-grained alumina [B8].

A crack in a component starts to propagate when the externally applied stress intensity factor K_{appl} exceeds the so-called crack tip toughness K_{I0}. For materials with a sufficiently steep R-curve, stable crack extension follows under increasing load. Failure of the component then occurs when the so-called tangent condition is fulfilled, i.e. when the slopes of $K_{appl}(a)$ and the R-curve $K_{IR}(a)$ are identical

$$K_{appl} = K_{IR} \quad , \quad \frac{dK_{appl}}{da} = \frac{dK_{IR}}{da} \qquad \text{(B3)}$$

Small natural flaws fail after a significantly shorter crack extension than long cracks (see e.g. [B9]).

From the failure condition (B3), it follows that the K_{Ic} value (i.e. the applied stress intensity factor K_{appl} at failure) must be different for small and large cracks (see [B9]), even if an

identical R-curve would exist for small and large cracks. In addition to this effect, the different types of R-curves make it indispensable to study the failure-relevant crack behaviour directly on small cracks.
As an appropriate test specimen, a bending bar with a very short and sharp notch with an extremely small notch root radius was developed. If the notch root radius is smaller or much smaller than the mean grain size, pre-existence of a “sharp” starter crack is ensured. For small starter cracks in the order of natural flaws (10-100µm) introduced by manufacturing and surface treatment, the fracture toughness is expected to reflect the behaviour of natural cracks, as is required for reliable strength predictions.

B2. Trapezoidal test specimen

Using the focussed ion beam microscope (FIB), it is possible to cut notches into microscopic specimens with notch root radii in the order of R<100 nm. Due to limitations of the total focussed ion beam sputtering time, specimen thicknesses are limited to about 0.6 mm and maximum notch depths are in the order of a<100 µm. In first experiments, notches of about 40µm depth were introduced.
The macroscopic specimen geometry shown in Fig. B3a was developed. The thickness on the tensile side of a trapezoidal bar, b, is in the order of 0.5mm, the thickness B at the compression surface is identical with the standard thickness of rectangular bending bars standing on end (B≈3mm). The width W also is a standard dimension of W≈4mm. It is usually applied for fracture toughness tests on edge-notched bars. This specimen can be loaded in the usual 4- and 3-point bending arrangements. A further modification that avoids tilting of the specimen during load application is shown in Fig. B3b, where the outer specimen parts remain rectangular. For a simpler handling, the purely trapezoidal bar can be supported on the thicker cross-section side, i.e. with the inner rollers as supports and the outer ones for the load application in the testing machine (Fig. B3c). For 3-point bending tests, Fig. B3d, it is recommended to glue the central cylinder to the lower piston. The upper rollers are mounted to the upper piston. During the test, the specimen is self-aligned exactly.
The edge notch was introduced with a focussed ion beam (FIB). By this procedure, notches of about 40 µm depth were produced. After the notching procedure, the specimens are ground again on the sides using SiC sand paper in order to remove the region where the scanning ion beam has affected the side surfaces.
In 4-point bending, the outer fibre tensile stress of the trapezoidal test specimen is

$$\sigma_{bend} = \frac{P(S_2 - S_1)}{4} \frac{12}{W^2} \frac{2B + b}{B^2 + 4Bb + b^2} \tag{B4}$$

with the dimensions given in Fig. B3.

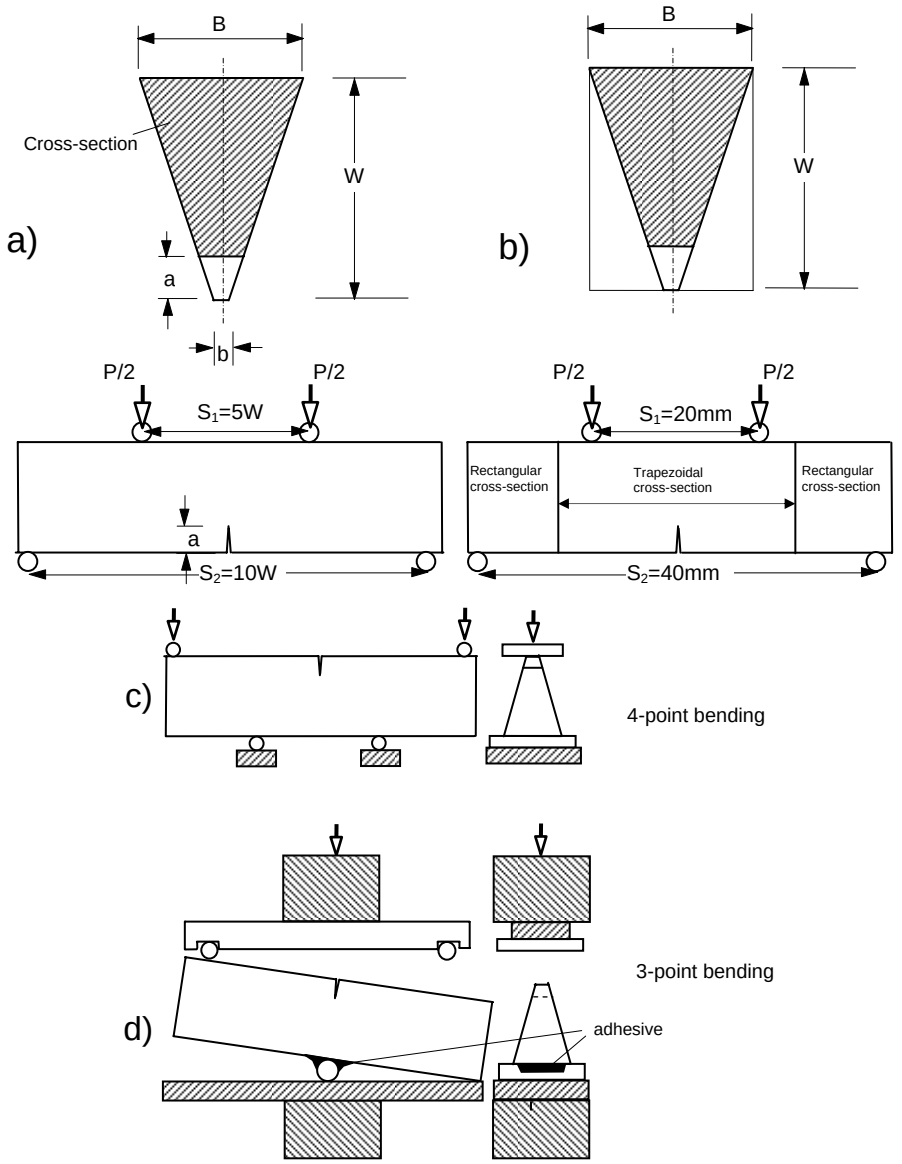

Fig. B3 a) 4-point bending test with a trapezoidal bar, b) specimen of variable cross-section, c) recommended arrangement for 4-point loading, d) for 3-point loading.

The stress intensity factors for several relative crack depths a/W and thickness ratios b/B were computed in a 3-dimensional finite element study. An eighth of the specimen was modeled with 10000 elements and 45000 nodes. For the crack tip region, 20-node elements - collapsed at the crack tip - were used. The stress intensity factors for a Poisson's ratio of $\nu=0.25$ were computed with ABAQUS Version 6.3 and expressed via the geometric function F defined in eq.(B1).

In Fig. B4a the geometric function is shown as a function of the location along the crack front. The maximum stress intensity factor is found in the crack centre, where plane strain conditions are fulfilled. Near the side surfaces, the stress intensity factor decreases significantly. The maximum stress intensity factor is plotted in Fig. B4b versus the geometric parameters b/B and a/W. The ratio B/W was chosen to be ¾, since standard test bars commonly have cross-sections of 3mm×4mm. The geometric function for the maximum stress intensity factor occurring at the symmetry axis tends to $F_{max}\cong 1.135$ for $a/W\to 0$ (dashed

curves in Fig. B4b). This value is only 1% higher than the 2-d solution of an edge-cracked half-space.

The description of near-tip stress fields by the stress intensity factor *K* is limited at the side surfaces. Near the intersection of the crack and the side surfaces, the singularity deviates from the ½ singularity valid for conventional stress intensity factors (Benthem [B10], Bazant and Estenssoro [B11], Dimitrov et al. [B12]).

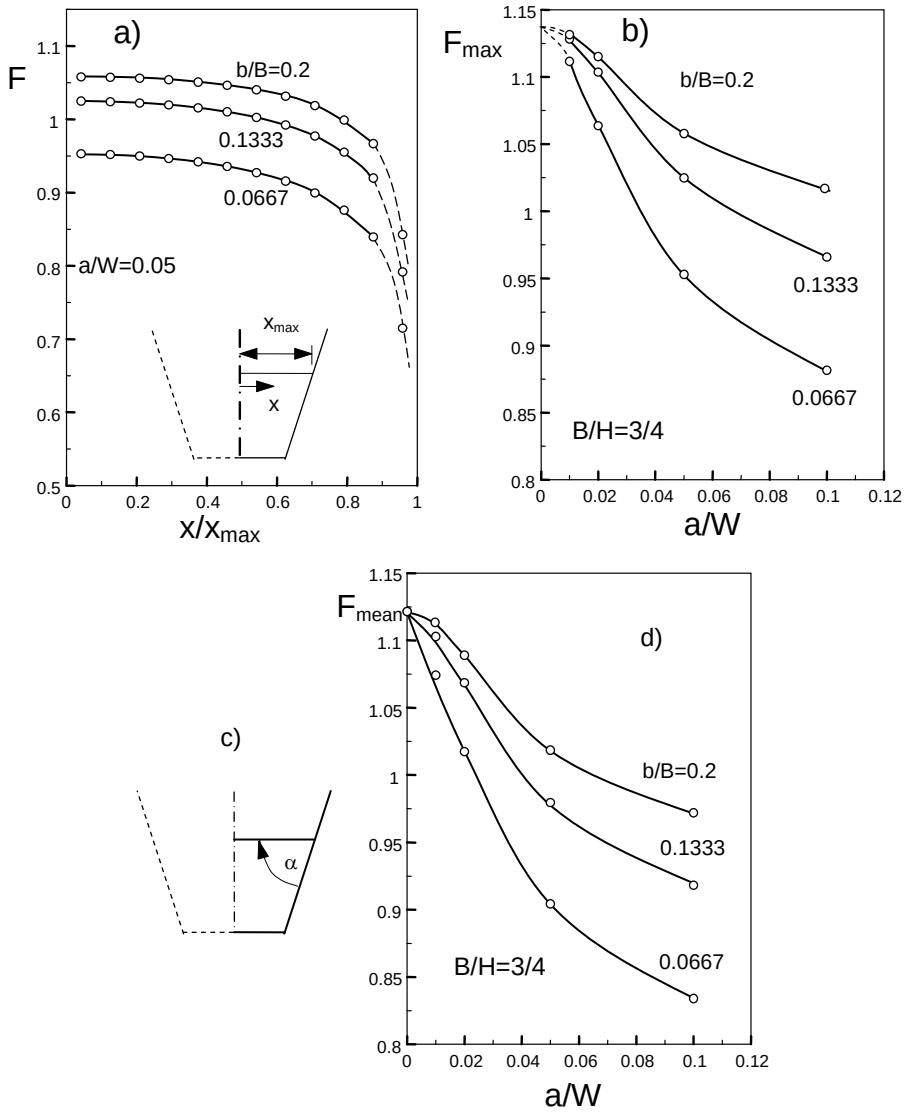

Fig. B4 Stress intensity factor along the crack front for ν=0.25, b) geometric function for maximum stress intensity factors occurring in the crack centre, c) definition of the crack-terminating angle α, d) geometric function for stress intensity factors averaged over the crack front.

The stresses at the distance *r* from the crack end point at the side surface are given as

$$\sigma_{ij} \propto r^{1-\lambda} \tag{B5}$$

with the singularity exponent λ depending on the angle α between crack and side surface (for the definition of the crack-terminating angle α, see Fig. B4c). In our case, the angle between

crack and side surface is about 71°. For this angle, Dimitrov et al. [B12] found a singularity exponent of $\lambda \approx 0.6$. This is a so-called weak singularity.
It should be emphasized that the singularity deviating from $\lambda = ½$ is not a special feature of the trapezoidal test specimen. It is present in any 3-dimensional crack-containing test sample and, thus, also a problem in the V-notched bar with a straight crack resulting in a crack-terminating angle of 90° (i.e. normal to the side surface) and, consequently, in a singularity exponent of $\lambda = 0.57$. This fact that is responsible for a disappearing stress intensity factor in the surface region has been nearly completely ignored by experimental investigations. The specimens are considered pure 2-d problems described by 2-d stress intensity factor solutions which are constant along the crack front. Only in the case of cracks with a terminating angle of about 100° (slightly depending on the Poisson's ratio ν), does the stress exponent have a constant value of $\lambda = 0.5$ along the whole crack front.
In order to reduce the side surface effect, let us define the mean stress intensity factor as the average over 90% of the crack, excluding the surface region in which the stress singularity deviates from the ½ singularity by

$$F_{mean} = \frac{1}{0.9x_{\max}} \int_0^{0.9x_{\max}} F(x)dx \qquad \text{(B6)}$$

Figure B4d represents the average geometric function. For $a/W \to 0$, the well-known limit case of $F = 1.1215$ (edge-cracked half-space) results for any ratio of b/B.

B3. First experimental results

First experimental results were obtained for a commercial Ce-stabilised zirconia with a mean grain size of about 1.7 µm. For this material we obtained notch root radii of less than 20 nm. The toughness was found to be $K_{Ic} \approx 4.1$ MPa√m.

From the result we conclude that

- the toughness value of $K_{Ic} \approx 4.1$ MPa√m determined with the FIB-introduced notch is a value for a "sharp crack" (i.e. a correct toughness result) since the notch radius is clearly smaller than the mean grain size,
- the test specimen yields toughness data for naturally small cracks since the initial crack has a depth that is comparable with the size of surface cracks in components introduced by surface grinding,
- the measured value is moderately affected by the R-curve. It is clearly smaller than the saturation of the R-curve as obtained with macrocracks at about 10-13 MPa√m [B13], but larger than the K_{I0} value obtained from COD measurements for instance (about 1.6-2.4 MPa√m).

References of Part B

B1 Nishida, T., Pezzotti, G., Mangialardi, T., Paolini, A.E., Fracture mechanics evaluation of ceramics by stable crack propagation in bend bar specimens, Fract. Mech. Ceram. **11**, (1996), 107–114.

B2 Kübler, J., Fracture toughness using the SEVNB method: Preliminary results, Ceramic Engineering & Science Proceedings, Vol. 18, (1997), 155-162.

B3 Fett, T., Munz, D., Stress Intensity Factors and Weight Functions, Computational Mechanics Publications, (1997), Southampton.

B4 Damani R., Gstrein, R., Danzer, R. ,Critical notch-root radius effect in SENB-S fracture toughness testing, J. E,op. Ceram. Soc. 16, pp. 695-702, 1996.

B5 Damani, R.J., Schuster, C., Danzer, R., Polished notch modification of SENB-S fracture toughness testing, J. Europ. Ceram. Soc. **17**(1997), 1685-1689.

B6 Munz, D., What can we learn from R-curve measurements? J. Am. Ceram. Soc. 90(2007), 1-15.

B7 Marshall, D.B., Swain, M.V., Crack resistance curves in magnesia-partially-stabilized zirconia, J. Am. Ceram. Soc. **71** (1988), 399–407.

B8 Steinbrech, R., Schmenkel,O., Crack resistance curves for surface cracks in alumina, Comm. J. Am. Ceram. Soc. **71**(1988), C271–C273.

B9 Munz, D., Fett, T., *CERAMICS, Failure, Material Selection, Design*, Springer-Verlag, (1999).

B10 Benthem, J.P., State of stress at the vertex of a quarter-infinite crack in a half-space. Int. J. of Solids and Structures, 13(1977), 479–492.

B11 Bazant, Z.P., Estenssoro, L.F., Surface singularity and crack propagation, Int. J. of Solids and Structures, 15 (1979), 405–426.

B12 Dimitrov, A., Buchholz, F.-G., Schnack, E., 3D-corner effects in crack propagation. In H.A. Mang, F.G. Rammerstorfer, and J. Eberhardsteiner, editors, *On-line Proc. of the 5th World Congress in Comp. Mech. (WCCMV)*, Vienna, Austria, July 7–12 2002. http://wccm.tuwien.ac.at/ index.html.

B13 Rauchs, G., Fett, T., Munz, D., R-curve behaviour of 9Ce-TZP zirconia ceramics, Engng. Fract. Mech. 69(2002), 389-401.

PART C

Multiple use of survived specimens in lifetime tests

C1. Subcritical crack growth

A crack of initial depth a_i propagates slowly, until a critical load-dependent size a_c is attained at which unstable crack extension follows. Crack growth is governed only by the stress intensity factor K. For a given material and environment, a unique relation between the crack growth rate v and K_I exists

$$v = \frac{da}{dt} = f(K_I)\,. \tag{C1}$$

Very often, the crack growth rates fulfil a power-law relation

$$v = AK_I^n = A^*\left(\frac{K_I}{K_{Ic}}\right)^n \tag{C2}$$

with the parameters A, A^* and n depending on the material, the temperature, and the environment.

The crack growth relation is very often determined in static lifetime tests. Especially for materials with a large crack growth exponent of e.g. n>50, the number of spontaneous failures during load application and survivals (tests in which a certain maximum time is exceeded) is larger than the number of tests with regular failure.

Sometimes, the surviving specimens are subjected to inert strength tests again. In order to obtain additional information on the subcritical crack growth behaviour, the authors recommend to perform lifetime tests on an increased load level. The related procedure will be outlined below. First, the procedure will be explained for the simple case of the power-law crack growth relation according to (C2). Then, it will be applied to static lifetime measurements on SIALON in distilled water of 20°C.

C2. Lifetimes under an arbitrary load history

C2.1 General lifetime relation

From the definition of the stress intensity factor and the power-law relation of subcritical crack growth, (C2), and under the assumption of a constant geometric function Y,

$$dt = \frac{1}{A\sigma^n Y^n a^{n/2}}\,da \tag{C3}$$

is obtained. Integration of (C2) from the initial crack depth a_i to the critical value a_c yields for arbitrary time-dependent stresses $\sigma(t)$

$$\int_0^{t_f} \sigma(t)^n\,dt = \frac{2}{AY^n(n-2)}\left[a_i^{\frac{2-n}{2}} - a_c^{\frac{2-n}{2}}\right]. \tag{C4}$$

Under the assumption of the lifetime and the strength being caused by the same flaws, the initial crack depth a_i can be derived directly from the so-called inert strength σ_c (i.e. the strength without influence of subcritical crack growth) and from the fracture toughness K_{Ic}

$$a_i = \left(\frac{K_{Ic}}{\sigma_c Y} \right)^2 . \tag{C5}$$

The inert strength σ_c may be determined by a test at high loading rate. An inert environment (e.g. vacuum) may additionally suppress subcritical crack growth.

Between the critical crack depth a_c and the stress at the moment of failure σ_f, the following relation holds:

$$a_c = \left(\frac{K_{Ic}}{\sigma_f Y} \right)^2 . \tag{C6}$$

Equation (C4) then reads

$$\int_0^{t_f} \sigma(t)^n \, dt = B \sigma_c^{n-2} \left[1 - (a_i / a_c)^{\frac{n-2}{2}} \right] \tag{C7a}$$

or

$$\int_0^{t_f} \sigma(t)^n \, dt = B \sigma_c^{n-2} [1 - (\sigma_f / \sigma_c)^{n-2}] \tag{C7b}$$

(see e.g. C1) with a material parameter B comprising some fracture mechanics quantities

$$B = \frac{2}{AY^2(n-2)} K_{Ic}^{2-n} = \frac{2K_{Ic}^2}{A^* Y^2 (n-2)} . \tag{C8}$$

The commonly applied lifetime tests are carried out under a constant load, as illustrated in Fig. 1a. In this case, the lifetime t_f results as

$$t_f = \frac{2K_{Ic}^2}{A^* Y^2 (n-2) \sigma^n} \sigma_c^{n-2} [1 - (\sigma_1 / \sigma_c)^{n-2}] \cong \frac{2K_{Ic}^2}{A^* Y^2 (n-2) \sigma^n} \sigma_c^{n-2} \tag{C9}$$

C2.2 Lifetimes under a step-shaped load history

A series of lifetime tests is performed at a stress level σ_1. After the time t_0, the load is increased to a stress level of σ_2. The load history (Fig. C1b) reads

$$\sigma(t) = \sigma_1 + (\sigma_2 - \sigma_1) \Theta(t - t_0) . \tag{C10}$$

(with the Heavyside step function Θ) or, equivalently,

$$\sigma(t) = \begin{cases} \sigma_1 & \text{for } t \le t_0 \\ \sigma_2 & \text{for } t > t_0 \end{cases} \tag{C11}$$

Inserting (C10) or (C11) into (C7b) yields

$$\sigma_1^n t_f = \frac{2K_{Ic}^2}{A^* Y^2 (n-2)} \sigma_c^{n-2} [1 - (\sigma_1 / \sigma_c)^{n-2}] \quad \textit{for} \quad t_f \le t_0 \tag{C12}$$

and

$$\sigma_1^n t_0 + \sigma_2^n (t_f - t_0) = \frac{2K_{Ic}^2}{A^* Y^2 (n-2)} \sigma_c^{n-2} [1 - (\sigma_2 / \sigma_c)^{n-2}] \quad for \quad t_f > t_0 \qquad \text{(C13)}$$

(with Y=1.3 for semi-circular surface cracks).

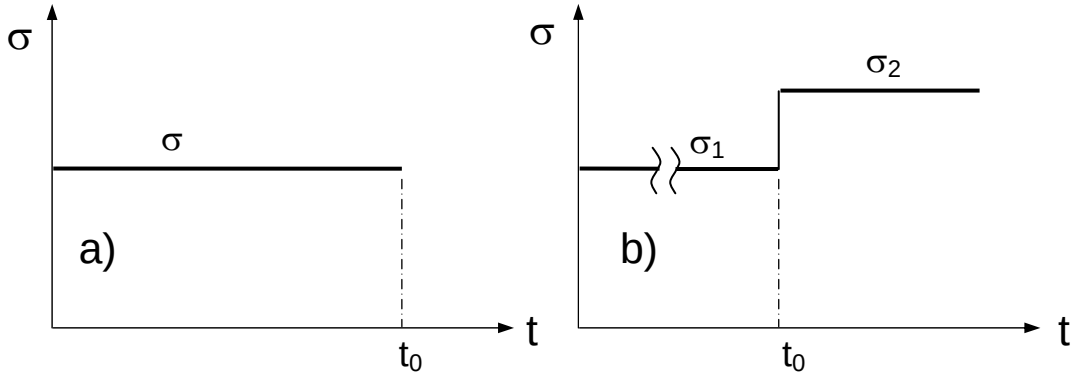

Fig. C1 Load-time histories for the lifetime tests, a) constant load σ, b) step-shaped load.

C3. Evaluation of tests with survivals

Let us now consider a lifetime test at load $\sigma=\sigma_1$. Some of the specimens may fail already during the loading step. Other specimens will fail before $t=t_0$ is reached, resulting in regular lifetimes t_f. Finally, after the time t_0, a few survivals will be found. For these specimens, the applied load is increased to $\sigma_2>\sigma_1$. The lifetime under σ_2 is determined. During load increase, also some of the specimens may fail immediately. This extended test is now defined as a lifetime test under step-shaped loading (Fig. C1b). The load on the first level is σ_1 and the time $t=t_0$ is the time limit defining the survivals of the first test.

From the system (C12) and (C13), the two parameters n and A^* can be determined, for instance, by using a least-squares procedure. It is assumed that a number of N samples are tested at high loading rates in an inert environment to give the strength distribution with the individual values $\sigma_{c,i}$. In a second series, also involving N specimens, the individual lifetimes $t_{f,i}$ are measured. The results are also arranged in increasing order.

With an arbitrarily chosen set of parameters (A^*, n), a series of lifetimes can be computed for the N tested samples, resulting in the distribution of $t_{f,computed,i}$. From (C12) and (C13), these lifetimes result as

$$t_{f,computed,i} = \frac{2K_{Ic}^2}{A^* Y^2 (n-2) \sigma_1^n} \sigma_{c,i}^{n-2} [1 - (\sigma_1 / \sigma_{c,i})^{n-2}] \quad \text{for} \quad \sigma_f = \sigma_1 \qquad \text{(C14)}$$

$$t_{f,computed,i} = \frac{2K_{Ic}^2}{A^* Y^2 (n-2) \sigma_2^n} \sigma_c^{n-2} [1 - (\sigma_2 / \sigma_c)^{n-2}] - \left(\frac{\sigma_1}{\sigma_2}\right)^n t_0 \quad \text{for} \quad \sigma_f = \sigma_2 \qquad \text{(C15)}$$

where $t_{f,computed,i}$ in (C15) is the time cumulated on the upper load level exclusively, i.e. $t_{f,total}$-t_0. The individual computed and measured lifetimes are then fitted by minimizing the deviations between the two quantities. This can, for instance, be done by

$$\sum_{i=1}^{N}\left(\frac{t_{f,computed,\mathrm{i}}}{t_{f,measured,\mathrm{i}}}-1\right)^2=\min \qquad \text{(C16a)}$$

or

$$\sum_{i=1}^{N}\left(\log\frac{t_{f,computed,\mathrm{i}}}{t_{f,measured,\mathrm{i}}}\right)^2=\min \qquad \text{(C16b)}$$

where the second expression takes into consideration the power law-shaped lifetime behaviour. This numerical treatment requires special experience in programming, since negative values of $t_{\mathrm{f,compute,i}}$ have to be avoided.

In order to vary the parameters n and A^* systematically, a FORTRAN program is used, based on the Harwell computer subroutine VA02AD.

If a sufficiently large number of survivals is available after the tests on stress level σ_2, the procedure can be repeated on an increased stress level $\sigma_3>\sigma_2$. Then, it results from (C7b) that

$$\sigma_1^n t_0+\sigma_2^n t_0+\sigma_3^n(t_f-t_0)=\frac{2K_{Ic}^2}{A^*Y^2(n-2)}\sigma_c^{n-2}[1-(\sigma_3/\sigma_c)^{n-2}] \quad for \quad t_f>t_0 \qquad \text{(C17)}$$

and

$$t_{f,computed,i}=\frac{2K_{Ic}^2}{A^*Y^2(n-2)\sigma_3^n}\sigma_c^{n-2}[1-(\sigma_3/\sigma_c)^{n-2}]-\left(\frac{\sigma_1}{\sigma_3}\right)^n t_0-\left(\frac{\sigma_2}{\sigma_3}\right)^n t_0 \qquad \text{(C18)}$$

C4. Experimental results

In order to apply the proposed procedure, lifetime measurements were carried out on SiAlON in water at room temperature.

Nd_2O_3 was used as a sintering additive in the starting powder mixtures for the fabrication of a mixed α/β-sialon. The composition investigated was calculated with the characteristic coefficients $m = 0.5$ and $n = 1.0$ (for details see [C2]). X-ray diffraction analysis of the samples showed an α/β ratio of 55/45. Sintering was performed in nitrogen atmosphere using a hot-isostatic press with a graphite resistance heater. The powder compacts were heated at a rate of 10K/min to the maximum sintering temperature of 1830°C, the pressure being 10 MPa. The thus obtained plates exhibited a relative density of 99.4% – 99.8% of the theoretical density.

From these plates, bars of 3mm × 4mm × 48mm in dimension were machined according to the European Standard EN 843-1:1995 for the 4-point-bending tests.

A number of N=27 inert strength tests were performed in air at a loading rate of about 100 **??**MPa/s. The strength distribution is shown in Fig. C2a in Weibull representation resulting in the Weibull parameters of

m=6.2 [4.6; 7.7], m_{corr}= 5.9, σ_0=904 MPa [854; 958]

These values were obtained by applying the maximum-likelihood procedure [C3]. The numbers in brackets are the 90% confidence intervals according to [C4] and m_{corr} is the un-biased Weibull exponent suggested by Thoman et al. [C3].

N=27 lifetime tests were performed at $\sigma=\sigma_1$ =700 MPa. During load application, 8 specimens failed spontaneously, 4 after regular lifetimes $t_f < t_0$ =280 h, and 15 specimens survived (circles in Fig. C2b). The load was then increased up to σ_2 = 800 MPa. Before this stress level was reached, a number of 5 specimens failed spontaneously. Of the remaining samples, 4 specimens failed during the next 280 hours (squares in Fig. C2b). Six specimens survived this second time span. The load was increased once more and the survivals were tested now at σ_3=900 MPa. Two specimens survived on this load level.

First, only the two lower load levels were evaluated. Application of eqs.(C14), (C15), and (C16b) resulted in

$$n=122.8,\ A^*=3.05\times10^{-2}\ \text{m/h} \qquad \text{(I)}$$

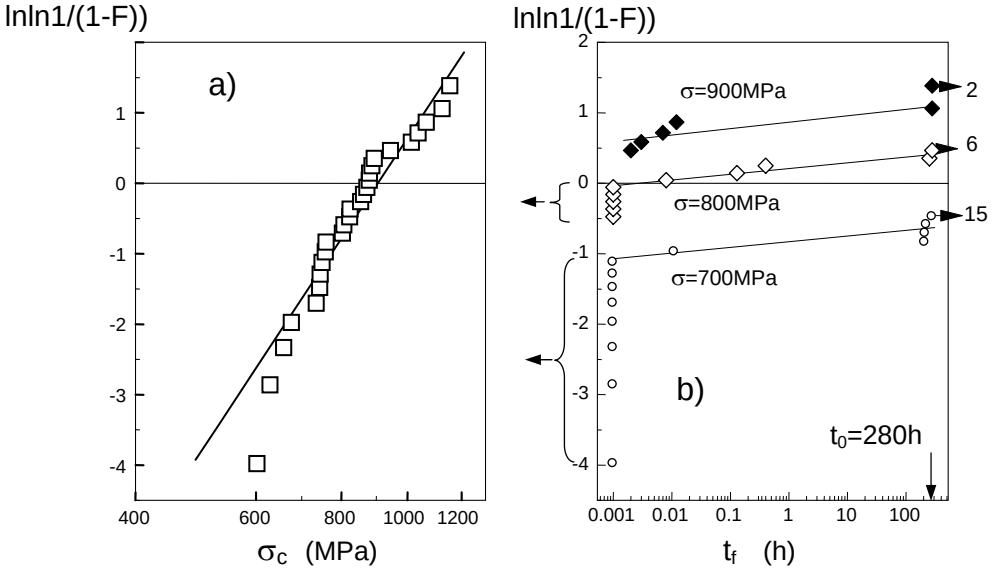

Fig. C2 a) Weibull representation of the inert strength, b) lifetimes (solid symbols: regular failure, symbols with arrows: fracture during loading or survivals).

In a second evaluation of all the load levels with an increased number of test results, the additional application of eq.(C18) yields

$$n=104.6,\ A^*=6.5\times10^{-3}\ \text{m/h} \qquad \text{(II)}$$

The solutions obtained from the evaluation of two and three load levels are represented in Fig. C3 by the straight lines. Since the higher n-value is related to the lower A^*, the two lines represent nearly the same region of data. In this context, it should mentioned that different solutions should always be assessed by the pair parameters and not by the individual n or A^* values.

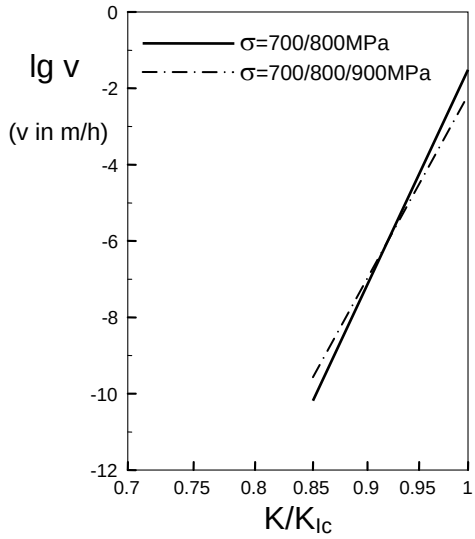

Fig. C3 Comparison of the power-law solutions obtained from the evaluation of the two lower stress levels (solid line) and the evaluation of all data (dash-dotted line).

C5. Modified lifetime evaluation without use of a power law assumption

C5.1 General description of the procedure

In Section C4, the measured lifetimes were evaluated in order to determine the *v*-*K* dependency of subcritical crack growth. The special assumption of a power-law relation was made. In most cases, this assumption is correct for ceramic materials and glass. A method which requires no assumption of the type of the relation $v=f(K)$ was proposed in [C5]. In this section, it will be shown how this method can be extended to lifetimes with repeated loading of survivals on a higher stress level. The general procedure will be explained for the case of tests on two different stress levels.

The lifetime in a static bending test at load σ_1, denoted as $t_{f,1}$, is given by

$$t_{f,1} = \frac{2}{\sigma_1^2 Y^2} \int_{K_i}^{K_{Ic}} \frac{K_I}{v(K_I)} dK_I \qquad \text{(C19)}$$

as outlined in detail in [C1, C5]. In (C19), K_i is the stress intensity factor at the moment of load application, i.e. the stress intensity factor corresponding to the initial crack size a_i

$$K_i = \sigma \sqrt{a_i} Y \,. \qquad \text{(C20)}$$

with $Y \cong 1.3$. Since the lifetime and the inert strength are caused by the same flaw population, it holds simply

$$K_i = \frac{\sigma}{\sigma_c} K_{Ic} \qquad \text{(C21)}$$

A series of N test specimens may be loaded at a stress of $\sigma=\sigma_1$. A number of p specimens will fail during load application and a number of q tests may lead to failure during the time $t=t_0$. The remaining number of N-p-q specimens survives at the load σ_1 reaching the time t_0 without fracture.

At time t_0 the actual stress intensity factor K_{sur} (subscript "*sur*" for survival) is given implicitly by the upper limit of the lifetime integral

$$t_0 = \frac{2}{\sigma_1^2 Y^2} \int_{K_i}^{K_{sur}} \frac{K_I}{v(K_I)} \mathrm{d}K_I \tag{C22}$$

The survivals are now used for lifetime tests on a higher stress level. By increasing the applied load from σ_1 to σ_2 the actual stress intensity factor is increased to the value

$$K_{re} = \frac{\sigma_2}{\sigma_1} K_{sur} \tag{C23}$$

where the subscript "*re*" stands for "re-start" of the lifetime test. Since any crack must have grown during the first loading period at $\sigma=\sigma_1$, it trivially holds $K_{sur}>K_i$, i.e.

$$K_{re} > \frac{\sigma_2}{\sigma_1} K_i \tag{C24}$$

During the re-loading step, a further number of *r* tests for which $K_{re} \geq K_{Ic}$ is fulfilled will fail spontaneously. The measurements carried out on the remaining number of *N-p-q-r* test specimens yields the lifetimes

$$t_{f,2} = \frac{2}{\sigma_2^2 Y^2} \int_{K_{re}}^{K_{Ic}} \frac{K_I}{v(K_I)} \mathrm{d}K_I \tag{C25}$$

(subscript "f,2" for failure at load level σ_2).

After introducing logarithmic derivations (for details, see [C1] or [C5]), differentiation of eqs.(C19) and (C25) with respect to the lower integration limits K_i and K_{re} yields the subcritical crack growth rates as a function of K_i and K_{re} as

$$v(K_i) = -\frac{2}{t_{f,1}\sigma_1^2} \left(\frac{K_i}{Y} \right)^2 \frac{d[\log(K_i / K_{Ic})]}{d[\log(t_{f,1}\sigma_1^2)]} \tag{C26}$$

and

$$v(K_{re}) = -\frac{2}{t_{f,2}\sigma_2^2} \left(\frac{K_{re}}{Y} \right)^2 \frac{d[\log(K_{re} / K_{Ic})]}{d[\log(t_{f,2}\sigma_2^2)]} \tag{C27}$$

It should be noted that in the logarithmic derivatives any constant factor, here K_{Ic}, may be introduced without effect on the derivative. This is due to the fact that the logarithm of a product with a constant term results in a sum with an additional term $\mathrm{d}[-\log(K_{Ic})]$ which disappears by taking the derivative.

The application of eq.(C27) needs knowledge of K_{re} and because of (C23) K_{sur} is necessary. Since only K_i is available from the inert strength according to (C21), the relation between K_{sur} and K_i has to be determined from (C22). Different strategies may be applied. The authors recommend and iterative procedure outlined in the following section.

C5.2 Lifetime evaluation

In order to provide realistic illustrations, let us use a somewhat complicated subcritical crack growth behaviour composed on a power-law relation followed by a plateau in crack growth

rates as may be present due to limited water diffusion near the crack tip. This behaviour is represented by

$$v = \begin{cases} A^*(K/K_{Ic})^n & \text{for} \quad K < K_{pl} \\ A^*(K_{pl}/K_{Ic})^n & \text{for} \quad K_{pl} \le K < K_{Ic} \\ \to \infty & \text{for} \quad K = K_{Ic} \end{cases} \tag{C28}$$

and illustrated in Fig. C4. As an example it is chosen for the lifetime computations: A^*=0.01 m/s, n=60, K_{pl}/K_{Ic}=0.85, and a toughness of K_{Ic}=4 MPa√m. For the inert strength distribution (necessary for the computation of realistic lifetimes) the Weibull parameters were selected to be m=8 and σ_0=800 MPa.

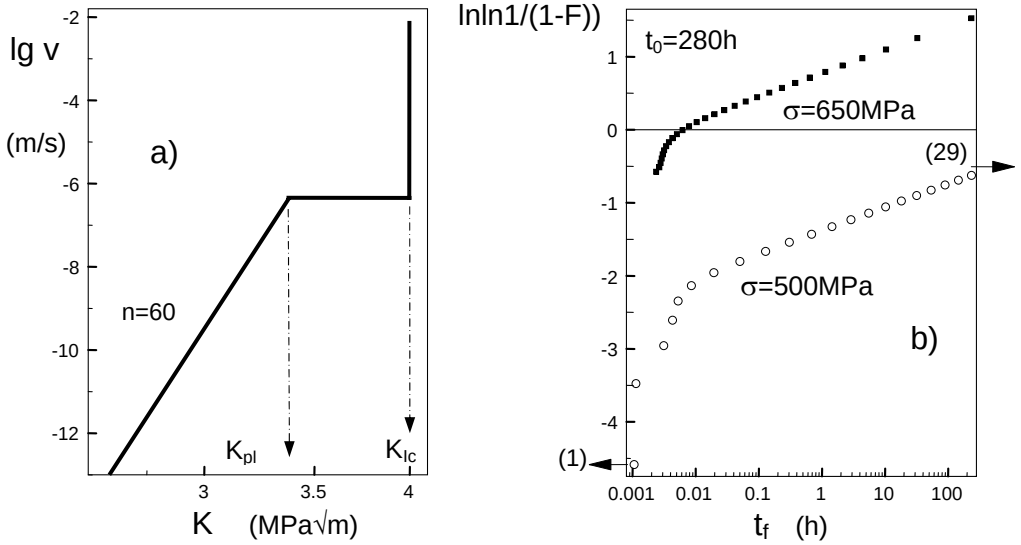

Fig. C4 a) Subcritical crack growth behaviour according to eq.(C28), b) lifetimes computed for σ_1=500 and σ_2=650 MPa (left arrow: spontaneous failure during loading, right arrow: survivals).

Figure C4b shows the lifetimes for two stress levels of σ_1=500 MPa and σ_2=650 MPa. They were computed by eqs.(C14) and (C15) for a limited maximum test duration of t_0=280h. At the lower load one specimen failed during load application, a number of 29 specimens survived.

Now let us forget the material data used for lifetime computations. For the demonstration of the evaluation procedure, the data of Fig. C4b are considered as experimental results without stochastic fluctuations.

A difficulty that complicates the procedure is the unknown re-loading stress intensity factor K_{re}. Its determination by eqs.(C23) needs the stress intensity factor K_{sur} of the survivals at the time t_0. On the other hand, evaluation of K_{sur} from eq.(C22) needs the solution $v(K)$ that is unknown so far. This fact calls for an iterative procedure.

Iteration step 1:

For a first estimation of K_{sur}, eqs.(C23) and (C24) suggest

$$K_{re}^{(1)} = \frac{\sigma_2}{\sigma_1} K_i \tag{C29}$$

where now the upper subscript indicates the first approximation.

In Fig. C5a the lifetimes of Fig. C4b are plotted versus the initial stress intensity factor K_i for the results obtained at σ_1. This diagram also contains the lifetimes at σ_2 as a function of $K_{re}^{(1)}$. The subcritical crack growth rates v were determined from eqs.(C26) and (C27). The logarithmic derivative was determined by use of Mathematica 3.0. Therefore, spline interpolation of the data in Fig. C5a was applied. The resulting first approximation of the v-K-curve is plotted in Fig. 5b.

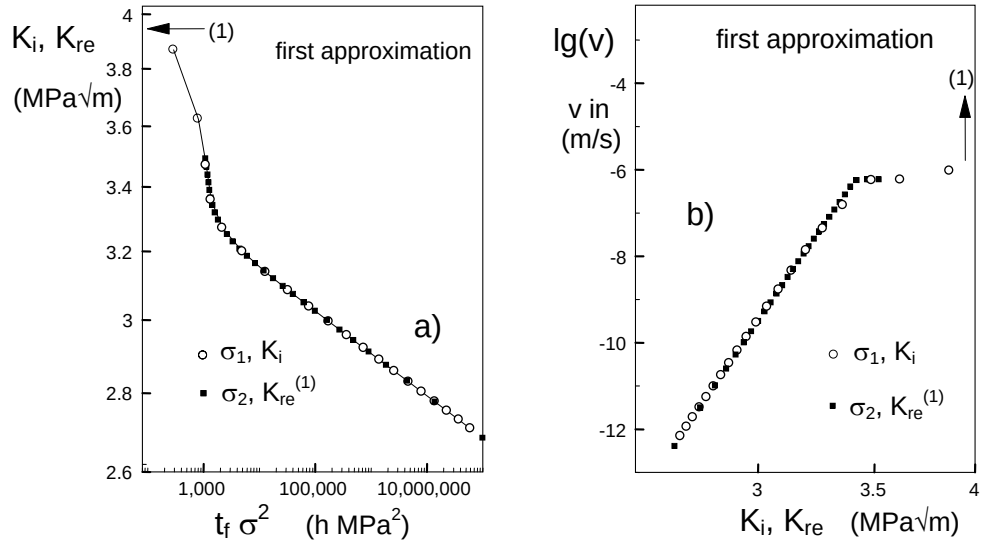

Fig. C5 First step of evaluation by setting $K_{re}=K_i\ \sigma_2/\sigma_1$; a) Stress intensity factors as a function of $t_f\ \sigma^2$, b) v-K-curve resulting from a) by application of eqs.(C26) and (C27).

Iteration step 2:

In this step now eq.(C22) can be solved, resulting in the relation $K_{re}^{(2)}=f(K_i)$. For this purpose the program module "FindRoot" of Mathematica is recommended with the integrand in (C20) represented by the interpolating function. The result of this evaluation is plotted in Fig. 6a. There exists nearly a unique relation $K_i=K_{re}$ as represented by the dashed straight line. Only for the 5-6 largest K_i-values a deviation from this line can be detected as illustrated in Fig. C6b.

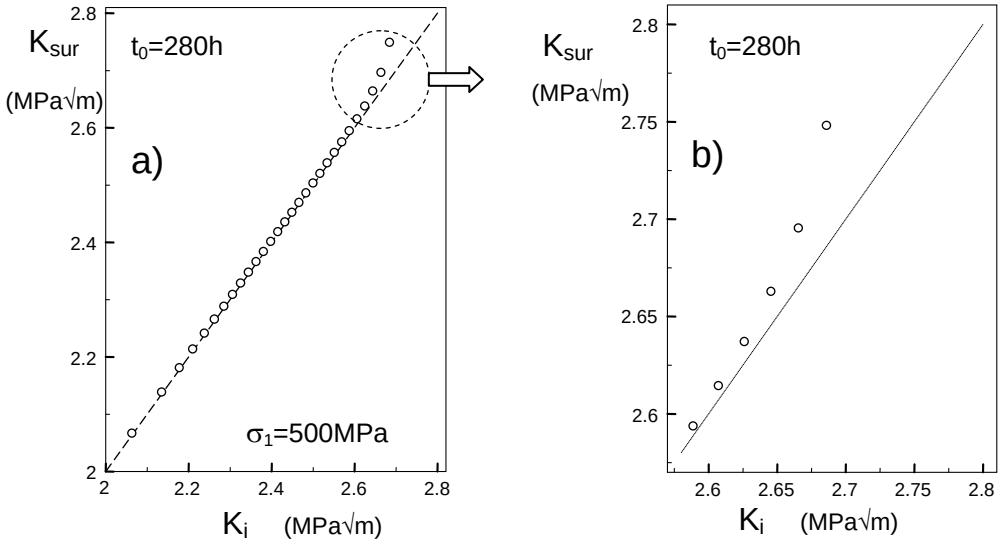

Fig. C6 a) Actual stress intensity factor K_{sur} of the survivals at σ_1 after the time t_0, b) detail of C6a.

The determination of the second approximation of the *v-K*-curve, the data of $K_{re}^{(2)}$ were used in eqs.(C23) and (C27).

The evaluation procedure in the second step of approximation is the same as for the first step. The auxiliary diagram $K_{re}=f(t_f\sigma^2)$ is therefore suppressed. In this context it has to be mentioned that the data obtained from the evaluation of the lower loading level remain unaffected. Only the data resulting from the re-loaded survivals have to be improved. Therefore, exclusively the data from the second load level are entered in Fig. C7.

An excellent agreement between the second approximation (diamond squares) and the prescribed *v-K*-relation given by eq.(C28) and introduced by the line. A determination of a third approximation makes no sense.

Having in mind the scatter in real lifetime measurements it can even be concluded that the first approximation is a sufficient representation of the *v-K* behaviour of a material. For ceramics with a rather low crack growth exponent *n* (e.g. $n<50$), the application of the second approximation may be suitable.

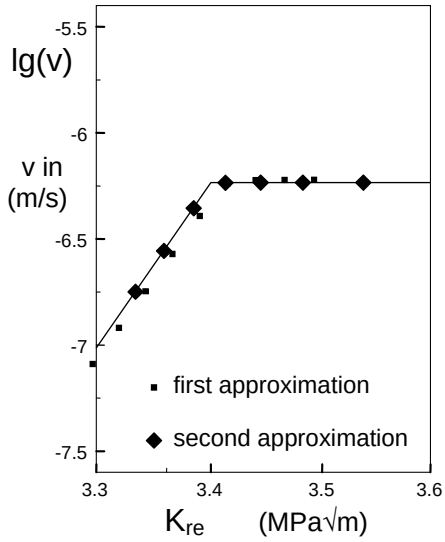

Fig. C7 Second approximation of the *v-K*-curve obtained from the re-loaded specimens (diamond squares) compared with the results from the first approximation (squares) and the v-*K* relation used for the computation of the "experimental" lifetimes (line).

C5.3 Application to the lifetime data measured on SiAlON

For the application of the method, lifetimes computed before with a prescribed crack growth law were used in Section C5.1. This was done in order to avoid disturbing statistical effects. Now, the measured data of Fig. C2 will be considered. Figure C8a shows the dependency between the lifetime quantity $t_f\sigma^2$ for σ_1=700 MPa (circles) and σ_2=800 MPa. The related *v-K* data are plotted in Fig. C8b. The straight line is the result obtained in Fig. C3 under the assumption of a power law according to eq.(C2). Except for the scatter of the individual data points, the agreement of the two methods is satisfactory.

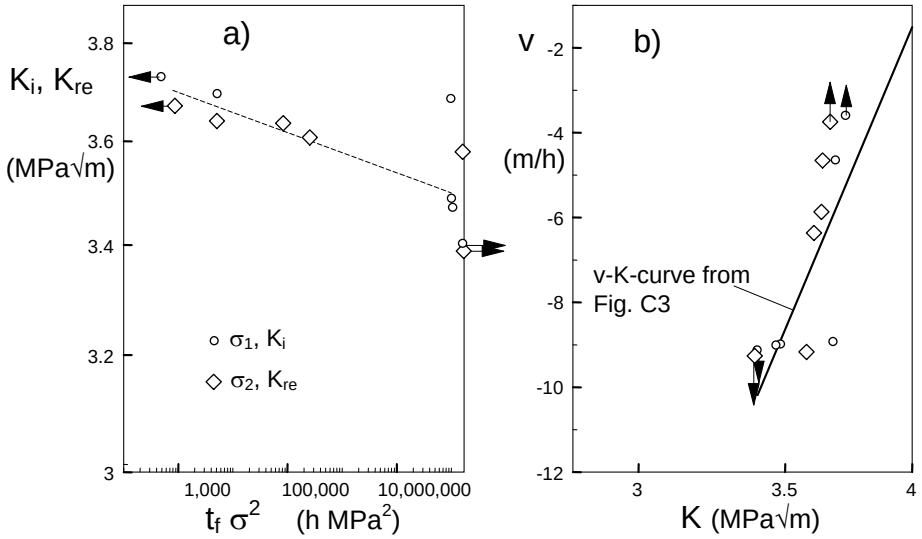

Fig. C6 Determination of the *v-K* curve for SiAlON; a) stress intensity factors K_i and K_{re}, b) *v-K* data (straight line: evaluation under the assumption of a power-law relation according to eq.(C2)).

References of Part C

C1 Munz D, Fett T, *CERAMICS, Failure, Material Selection, Design*, Springer-Verlag, (1999).

C2 Holzer, S., Geßwein, H., Hoffmann, M.J., Phase relationships in Neodymia- and Ytterbia-containing SiAlONs. Key Eng. Mat., **237**, (2003), 43-48.

C3 Thoman, D.R., Bain, L.J., Antle, C.E., Inferences on the parameters of the Weibull distribution, Technometrics **11**, (1969) 445.

C4 European Standard ENV 843-5, Advanced monolithic ceramics – mechanical tests at room temperature – statistical analysis.

C5 Fett, T., Munz, D., Determination of v-K_I-curves by a modified evaluation of lifetime measurements in static bending tests, Comm. Am. Ceram. Soc. **68** (1985), C213–C215.